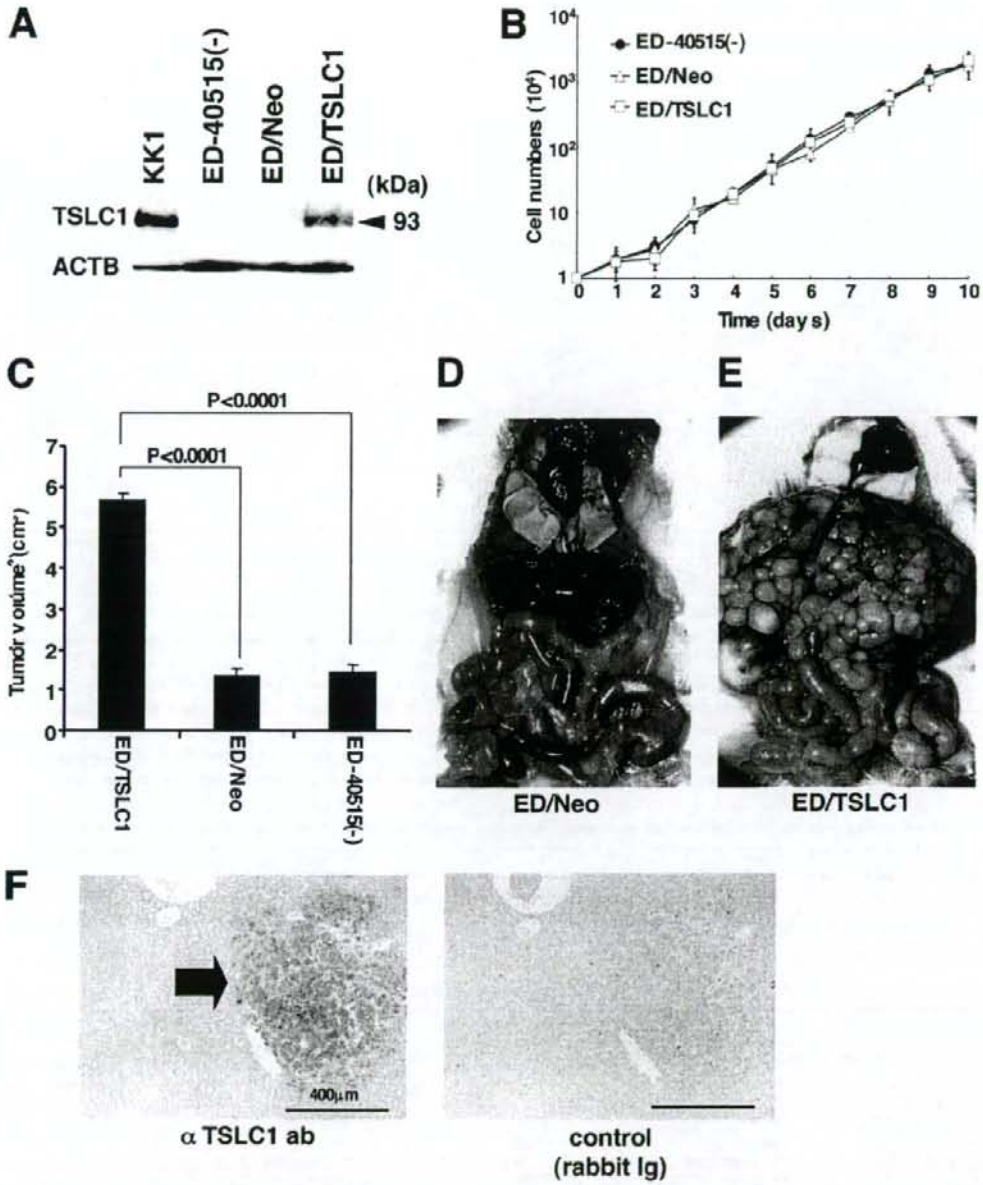

FIG. 2. Involvement of TSLC1 expression in tumor growth and infiltration of leukemia cells in NOG mice. (A) Expression of TSLC1 in KK1, ED-40515(−), ED/Neo, or ED/TSLC1 cell lines was detected by Western blot analysis. Expression of β-actin protein (ACTB) was used as a loading control. (B) Cell growth curves of ED-40515(−), ED/Neo, and ED/TSLC1 cell lines are shown for an average of three independent counts, and standard deviations are indicated as error bars. (C) Tumor volumes of mice inoculated subcutaneously with ED/TSLC1, ED/Neo, or ED-40515(−) cells after 21 days are shown as the means ± standard errors of the means for five mice in each group. Statistical analysis was done with a Student *t* test. (D and E) The pictures shown were derived from gross photographs of the sacrificed mice at 1 month after intravenous inoculation of ED/Neo (D) or ED/TSLC1 (E) cells. (F) Immunohistochemical staining for TSLC1 protein in liver metastases of the mice inoculated intravenously with ED/TSLC1 cells is shown. An arrow indicates a tumor mass with strong staining with a rabbit anti-TSLC1 antibody; however, the same mass shows no staining with rabbit immunoglobulin (Ig) as a negative control. Magnification, ×100; bars, 400 μm.

TABLE 1. Invasion scores of mice inoculated with ED/Neo or ED/TSLC1 cells

Cell line and mouse	Invasion score for organ by observation:									
	Macroscopic[a]					Microscopic[b]				
	Liver	Kidney	Lung	Ovary	Spleen	Liver	Kidney	Lung	Ovary	Spleen
ED/TSLC1										
T1	3+	−	+/−	1+	−	3+	−	2+	2+	−
T2	3+	−	−	1+	−	3+	−	2+	2+	−
T3	3+	−	+/−	2+	−	3+	−	2+	2+	−
T4	3+	−	−	1+	−	3+	−	2+	2+	−
T5	2+	−	−	2+	−	3+	−	2+	3+	−
T6	3+	−	+/−	1+	−	3+	−	+/−	2+	−
ED/Neo										
N1	−	−	−	2+	−	2+	−	+/−	3+	−
N2	+/−	−	−	1+	−	+/−	−	−	2+	−
N3	−	−	−	2+	−	−	−	+/−	2+	−
N4	−	−	−	1+	−	−	−	−	2+	−
N5	−	−	−	1+	−	ND[c]	ND	ND	ND	ND
N6	−	−	−	1+	−	ND	ND	ND	ND	ND

[a] Subjective invasion scores by macroscopic observation were as follows: −, no invasion; +/−, less than 10% invasion in the organ; 1+, 10 to 30% invasion in the organ; 2+, 30 to 70% invasion in the organ; 3+, over 70% invasion in the organ.

[b] Subjective invasion scores by microscopic observation were as follows: −, no invasion; +/−, less than 1% leukemia cells in the section; 1+, less than 10% leukemia cells in the section; 2+, 10 to 30% leukemia cells in the section; 3+, over 30% leukemia cells in the section

[c] ND, not done.

detected by Western blot analysis (Fig. 1A). Expression of a TSLC1 protein in EL4/TSLC1 cells was also shown on Western blot analysis with KK1, an ATL cell line expressing TSLC1 (12) (Fig. 1B). In an in vitro cell growth assay, 2×10^4 cells were incubated, and their growth was analyzed by direct counting with trypan blue dye staining. EL4 and EL4/TSLC1 cells showed nearly identical proliferation profiles in vitro, while Tax-expressing EL4 cells proliferated more slowly (Fig. 1C). This difference in cell growth might be caused by different expression vectors. In an in vivo growth assay, 2×10^6 cells of each cell line were injected into the peritoneal cavity of C57BL/6J mice: eight mice for EL4 cells as controls, 13 mice for EL4/TSLC1 cells, and eight mice for EL4/GAX cells. All of the mice died of tumor invasion of various organs with ascitic fluids in 40 to 120 days. The median survival time of the control mice injected with EL4 cells or EL4/GAX cells was 72 days. The mice with EL4/TSLC1 cells, however, died within 60 days, with a median survival time of 41 days (Fig. 1D). The phenotypes of the control mice and the EL4/TSLC1 mice were almost identical with invasion of tumors into various organs. Organ metastasis of tumor cells in three EL4/TSLC1-inoculated mice, two EL4-inoculated mice, and one EL4/GAX-inoculated mouse was analyzed and evaluated with hematoxylin-eosin staining. The liver was one of the major sites of metastasis in all three of the EL4/TSLC1-inoculated mice by histopathological analysis but not in the two EL4-inoculated mice or the EL4/GAX-inoculated mouse (Fig. 1E). These results support the role of TSLC1 overexpression in T-lymphoma cells as one of an aggressive factor in the development of leukemia/lymphoma.

In order to investigate the possibility that overexpression of TSLC1 promotes tumor growth and/or infiltration in vivo,

TABLE 2. Clinical characteristics of patients and pathological findings of organ invasion[a]

Patient no.	Age (yr)/sex	Clinical characteristic				Invasion score in NOG mice[b]				TSLC1 expression score[c]
		Diagnosis (ATL type)	WBC (10^9/liter)	Lymphocytes (%)	Atypical cells (%)	Liver	Lung	Spleen	Lymph node	
1	73/M	Chronic	7.8	59	47	3+	3+	3+	ND	3+
2	59/F	Chronic	9.0	75	40	3+	2+	2+	1+	2+
3	66/F	Chronic	29.4	49	75	3+	3+	3+	ND	3+
4	44/F	Chronic	22.6	51	45	3+	2+	2+	2+	2+
5	43/F	Chronic	18.6	63	43	3+	3+	3+	ND	2+
6	54/M	Acute	192.8	65	91	1+	2+	ND	ND	1+
7	58/M	Acute	67.3	71	80	3+	3+	3+	ND	2+
8	65/F	Acute	29.4	25	60	3+	2+	ND	3+	3+
9	68/M	Acute	30.0	79	81	3+	1+	1+	2+	2+
10	66/F	Acute	10.2	38	51	3+	3+	3+	ND	3+

[a] Abbreviations: M, male; F, female; WBC, white blood cells; ND, not done.

[b] Subjective invasion scores were as follows; 0, no invasion; 1+, less than 10% leukemia cells in the section; 2+, 10 to 30% leukemia cells in the section; 3+, over 30% leukemia cells in the section.

[c] Subjective scores of TSLC1 expression in pathological immunostaining were as follows; −, no staining; 1+, faint staining in less than 10% of invasive leukemia cells; 2+, weak to moderate staining in 30 to 70% of invasive leukemia cells; 3+, intense staining in more than 70% of invasive leukemia cells.

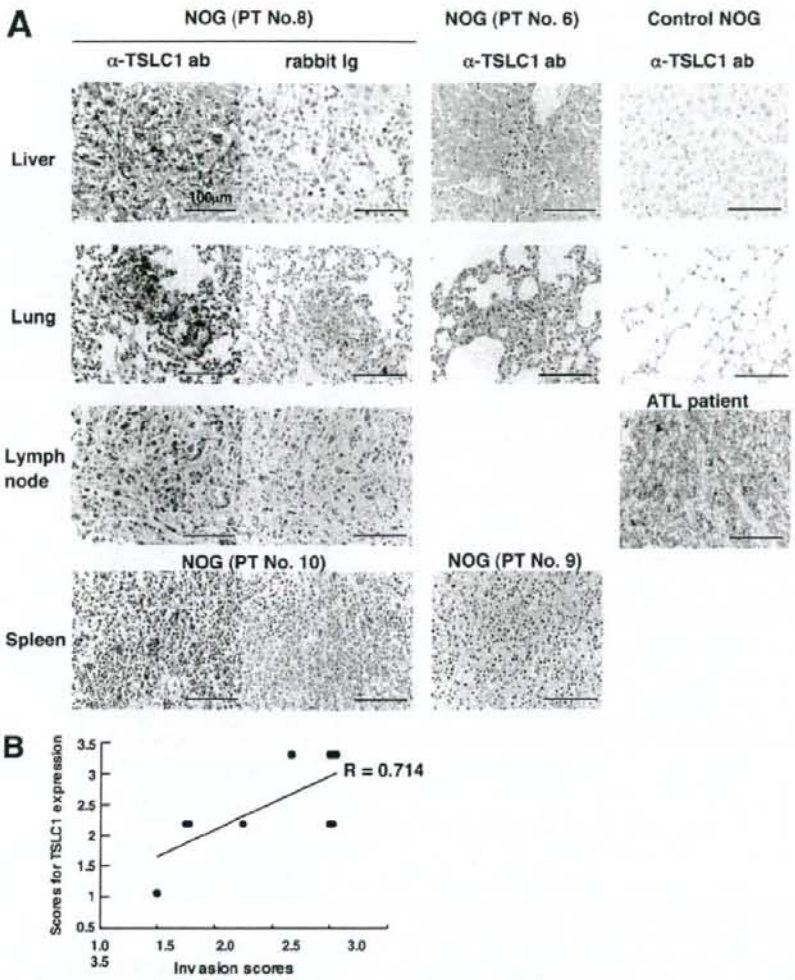

FIG. 3. Growth and infiltration of primary ATL cells in various organs of NOG mice based on TSLC1 expression. (A) Immunohistochemical staining of various organs of NOG mice inoculated with leukemia cells from patient 6, 8, 9, or 10 is shown with the use of rabbit anti-TSLC1 antibody or rabbit immunoglobulin (Ig) as a negative control. Sections from patients 8 and 10 showed severe invasion (invasion score, 3) and dense staining for TSLC1 (expression score, 3), while sections from patients 6 and 9 showed mild invasion (invasion score, 1) and light staining for TSLC1 (expression score, 1). Liver and lung sections from control NOG mice were used as negative controls, and a lymph node from an ATL patient was used as a positive control. Magnification, ×400; bars, 100 μm. (B) The diagram of dispersion between mean values of each invasion score and scores for TSLC1 expression in each NOG mouse inoculated with primary ATL cells showed moderate correlation ($R = 0.714$).

ATL-derived ED-40515(−) cells (10) were injected into NOG mice. Since expression of TSLC1 in ED-40515(−) cells is severely reduced by promoter methylation, they were transfected with either a TSLC1 expression plasmid (pcDNA3/TSLC1) or a mock plasmid (pcDNA3/Neo). ED/TSLC1 and ED/Neo cells were identified by selection with G-418. High levels of TSLC1 expression were verified in the ED/TSLC1 cells, but not in the ED/Neo cells, by Western blot analysis (Fig. 2A). The ED/TSLC1, ED/Neo, and ED-40515(−) cell lines all showed the same proliferation profile in vitro (Fig. 2B). Cells (10×10^6) were inoculated subcutaneously into the postauricular region of NOG mice, which permitted the observation of tumor growth macroscopically and the measurement of tumor size over a relatively short time (3). The ED/TSLC1 cell lines caused greater formation of larger tumors than did the ED/Neo and ED-40515(−) cell lines (Fig. 2C). The development of clinical signs of near-death (e.g., piloerection, weight loss, and cachexia) in mice at the time of killing was also more prevalent with the ED/TSLC1 cell line. These results suggest that TSLC1 expression in ATL cells enhances in vivo tumor growth in NOG mice.

Since the mice died within 4 weeks after subcutaneous in-

oculation of leukemia cells due to heavy tumor burden, 2×10^6 ED/TSLC1 or ED/Neo cells were intravenously injected into six NOG mice in order to investigate their capacity for invasion of various organs. After 1 month, we sacrificed the mice to determine the extent of organ invasion. Macroscopically, all of the mice injected with ED/TSLC1 cells (six/six) showed severe liver invasion with swelling of the ovaries. None of the mice injected with ED/Neo cells showed liver invasion, but they did show ovarian involvement (Fig. 2D and E). Microscopically, all of the mice inoculated with ED/TSLC1 cells showed severe and massive liver and lung invasions. On the other hand, only one of six mice inoculated with ED/Neo cells showed a large amount of liver metastasis (Table 1). TSLC1 expression in tumor cells infiltrating the liver was confirmed by immunohistochemical staining (Fig. 2F). Thus, overexpression of TSLC1 in ATL cells might enhance organ invasion, and particularly invasion of the liver and lung.

Next, we examined whether primary ATL cells with various levels of expression of TSLC1 could efficiently grow and infiltrate various organs in NOG mice. TSLC1-positive primary ATL cells (2×10^7) from five acute-type and five chronic-type ATL patients were inoculated subcutaneously into the postauricular region of NOG mice (Table 2). All of the mice developed clinical signs of near-death (e.g., piloerection, weight loss, and cachexia) 6 to 8 weeks after inoculation, in addition to the enlargement of the lymph nodes, spleen, lungs, and liver. Microscopically, ATL cells invaded various organs of all ATL-bearing NOG mice to different degrees. Based on results of immunohistochemical staining for TSLC1, all invading leukemia cells expressed TSLC1 protein, compared with no TSLC1 expression in these organs in control NOG mice (Table 2 and Fig. 3A). The dispersion diagram for the levels of invasion and the levels of TSLC1 expression in the leukemia cells showed a correlation coefficient of 0.714, suggesting that there was a moderate correlation between invasive capability and the level of TSLC1 expression (Fig. 3B). Thus, TSLC1 could aid in the formation of a rapidly growing large tumor and massive infiltration of ATL cells into various organs in NOG mice. Since TSLC1 is expressed in various types of ATL cells, including smoldering and chronic types, it might be a promising target for the development of a new anti-ATL therapy. The NOG mouse model system described in the present study could provide a novel means by which to understand and investigate the further importance of TSLC1 in ATL progression.

We thank S. Ichinose of the Instrumental Analysis Research Center; S. Endo of the Animal Research Center, Tokyo Medical and Dental University; and Y. Sato of the National Institute of Infectious Diseases for her excellent technical assistance. Anti-Tax (MI73) antibody was the kind gift of Y. Namba and M. Matsuoka (Institute for Virus Research, Kyoto University).

Supported by grants from the Ministry of Education, Science, and Culture; the Ministry of Health, Labor, and Welfare; and Human Health Science of Japan.

REFERENCES

1. **Ballard, D. W., E. Bohnlein, J. W. Lowenthal, Y. Wano, B. R. Franza, and W. C. Greene.** 1988. HTLV-I tax induces cellular proteins that activate the B element in the IL-2 receptor gene. Science **241**:1652–1655.
2. **Cross, S. L., M. B. Feinberg, J. B. Wolf, N. J. Holbrook, F. Wong-Staal, and W. J. Leonard.** 1987. Regulation of the human interleukin-2 receptor chain promoter: activation of a nonfunctional promoter by the transactivator gene of HTLV-I. Cell **49**:47–56.
3. **Dewan, M. Z., K. Terashima, M. Taruishi, H. Hasegawa, M. Ito, Y. Tanaka, N. Mori, T. Sata, Y. Koyanagi, M. Maeda, Y. Kubuki, A. Okayama, M. Fujii, and N. Yamamoto.** 2003. Rapid tumor formation of human T-cell leukemia virus type 1-infected cell lines in novel NOD-SCID/$c\gamma^{null}$ mice: suppression by an inhibitor against NF-κB. J. Virol. **77**:5286–5294.
4. **Dewan, M. Z., J. N. Uchihara, K. Terashima, M. Honda, T. Sata, M. Ito, N. Fujii, K. Uozumi, K. Tsukasaki, M. Tomonaga, Y. Kubuki, A. Okayama, M. Toi, N. Mori, and N. Yamamoto.** 2006. Efficient intervention of growth and infiltration of primary adult T-cell leukemia cells by an HIV protease inhibitor, ritonavir. Blood **107**:716–724.
5. **Felber, B. K., H. Paskalis, C. Kleinman-Ewing, F. Wong-Staal, and G. N. Pavlakis.** 1985. The pX protein of HTLV-I is a transcriptional activator of its long terminal repeats. Science **229**:675–679.
6. **Furuta, R. A., K. Sugiura, S. Kawakita, T. Inada, S. Ikehara, T. Matsuda, and J. Fujisawa.** 2002. Mouse model for the equilibration interaction between the host immune system and human T-cell leukemia virus type 1 gene expression. J. Virol. **76**:2703–2713.
7. **Hinuma, Y., K. Nagata, M. Hanaoka, M. Nakai, T. Matsumoto, K. I. Kinoshita, S. Shirakawa, and I. Miyoshi.** 1981. Adult T-cell leukemia: antigen in an ATL cell line and detection of antibodies to the antigen in human sera. Proc. Natl. Acad. Sci. USA **78**:6476–6480.
8. **Ito, M., H. Hiramatsu, K. Kobayashi, K. Suzue, M. Kawahata, K. Hioki, Y. Ueyama, Y. Koyanagi, K. Sugamura, K. Tsuji, T. Heike, and T. Nakahata.** 2002. NOD/SCID/γcnull mouse: an excellent recipient mouse model for engraftment of human cells. Blood **100**:3175–3182.
9. **Kuramochi, M., H. Fukuhara, T. Nobukuni, T. Kanbe, T. Maruyama, H. P. Ghosh, M. Pletcher, M. Isomura, M. Onizuka, T. Kitamura, T. Sekiya, R. H. Reeves, and Y. Murakami.** 2001. TSLC1 is a tumor suppressor gene in human non-small cell lung cancer. Nat. Genet. **27**:427–730.
10. **Maeda, M., A. Shimizu, K. Ikuta, H. Okamoto, M. Kashihara, T. Uchiyama, T. Honjo, and J. Yodoi.** 1985. Origin of human T-lymphotrophic virus I-positive T cell lines in adult T cell leukemia. Analysis of T cell receptor gene rearrangement. J. Exp. Med. **162**:2169–2174.
11. **Maruyama, M., H. Shibuya, H. Harada, M. Hatakeyama, M. Seiki, T. Fujita, J. Inoue, M. Yoshida, and T. Taniguchi.** 1987. Evidence for aberrant activation of the interleukin-2 autocrine loop by HTLV-1-encoded p40x and T3/Ti complex triggering. Cell **48**:343–350.
12. **Masuda, M., M. Yagita, H. Fukuhara, M. Kuramochi, T. Maruyama, A. Nomoto, and Y. Murakami.** 2002. The tumor suppressor protein TSLC1 is involved in cell-cell adhesion J. Biol. Chem. **277**:31014–31019.
13. **Murakami, Y., T. Nobukuni, K. Tamura, T. Maruyama, T. Sekiya, Y. Arai, H. Gomyou, A. Tanigami, M. Ohki, D. Cabin, P. Frischmeyer, P. Hunt, and R. H. Reeves.** 1998. Localization of tumor suppressor activity important in non-small cell lung carcinoma on chromosome 11q. Proc. Natl. Acad. Sci. USA **95**:8153–8158.
14. **Poiesz, B. J., F. W. Ruscetti, A. F. Gazdar, P. A. Bunn, J. D. Minna, and R. C. Gallo.** 1980. Detection and isolation of type C retrovirus particles from fresh and cultured lymphocytes of a patient with cutaneous T-cell lymphoma. Proc. Natl. Acad. Sci. USA **77**:7415–7419.
15. **Sasaki, H., I. Nishikata, T. Shiraga, E. Akamatsu, T. Fukami, T. Hidaka, Y. Kubuki, A. Okayama, K. Hamada, H. Okabe, Y. Murakami, H. Tsubouchi, and K. Morishita.** 2005. Overexpression of a cell adhesion molecule, TSLC1, as a possible molecular marker for acute type of adult T-cell leukemia. Blood **105**:1204–1213.
16. **Sodroski, J. G., C. A. Rosen, and W. A. Haseltine.** 1984. Transacting transcriptional activation of the long terminal repeat of human T lymphotropic viruses in infected cells. Science **225**:381–385.
17. **Yamaguchi, K., and T. Watanabe.** 2002. Human T lymphotropic virus type-I and adult T-cell leukemia in Japan. Int. J. Hematol. **76**:240–245.
18. **Yoshida, M., I. Miyoshi, and Y. Hinuma.** 1982. Isolation and characterization of retrovirus from cell lines of human adult T-cell leukemia and its implication in the disease. Proc. Natl. Acad. Sci. USA **79**:2031–2035.

nature

Vol 456|13 November 2008|doi:10.1038/nature07383

LETTERS

Loss of the autophagy protein Atg16L1 enhances endotoxin-induced IL-1β production

Tatsuya Saitoh[1,3]*, Naonobu Fujita[4]*, Myoung Ho Jang[2], Satoshi Uematsu[1,3], Bo-Gie Yang[1,3], Takashi Satoh[1,3], Hiroko Omori[4], Takeshi Noda[4], Naoki Yamamoto[5], Masaaki Komatsu[6,7,8], Keiji Tanaka[6], Taro Kawai[1,3], Tohru Tsujimura[9], Osamu Takeuchi[1,3], Tamotsu Yoshimori[4,10] & Shizuo Akira[1,3]

Systems for protein degradation are essential for tight control of the inflammatory immune response[1,2]. Autophagy, a bulk degradation system that delivers cytoplasmic constituents into autolysosomes, controls degradation of long-lived proteins, insoluble protein aggregates and invading microbes, and is suggested to be involved in the regulation of inflammation[3–5]. However, the mechanism underlying the regulation of inflammatory response by autophagy is poorly understood. Here we show that Atg16L1 (autophagy-related 16-like 1), which is implicated in Crohn's disease[6,7], regulates endotoxin-induced inflammasome activation in mice. Atg16L1-deficiency disrupts the recruitment of the Atg12-Atg5 conjugate to the isolation membrane, resulting in a loss of microtubule-associated protein 1 light chain 3 (LC3) conjugation to phosphatidylethanolamine. Consequently, both autophagosome formation and degradation of long-lived proteins are severely impaired in Atg16L1-deficient cells. Following stimulation with lipopolysaccharide, a ligand for Toll-like receptor 4 (refs 8, 9), Atg16L1-deficient macrophages produce high amounts of the inflammatory cytokines IL-1β and IL-18. In lipopolysaccharide-stimulated macrophages, Atg16L1-deficiency causes Toll/IL-1 receptor domain-containing adaptor inducing IFN-β (TRIF)-dependent activation of caspase-1, leading to increased production of IL-1β. Mice lacking Atg16L1 in haematopoietic cells are highly susceptible to dextran sulphate sodium-induced acute colitis, which is alleviated by injection of anti-IL-1β and IL-18 antibodies, indicating the importance of Atg16L1 in the suppression of intestinal inflammation. These results demonstrate that Atg16L1 is an essential component of the autophagic machinery responsible for control of the endotoxin-induced inflammatory immune response.

Autophagy is a bulk degradation system, which controls the clearance and re-use of intracellular constituents, and is important for the maintenance of an amino acid pool essential for survival[3–5]. In addition, recent studies have disclosed multiple roles of autophagy in the regulation of cell death, differentiation and anti-microbial response in mammals[4,5]. Yeast genetic screening studies have identified a variety of essential components of autophagic machinery, called Atg proteins, which are phylogenetically highly conserved, and several mammalian counterparts, such as Atg5 and Atg7, have been reported[3–5]. Previously, we systematically characterized mammalian homologues of Atg proteins and identified Atg16L1 protein as an Atg5-binding protein[10]. Its coiled-coil domain, which mediates self-multimerization, is essentially required for starvation-induced autophagy in yeast, and this domain is conserved in mammalian Atg16L1 (refs 3, 10; Fig. 1a). We have proposed that the coiled-coil domain of Atg16L1 is required for the formation of an ~800 kDa high molecular weight protein complex with the Atg12-Atg5 conjugate and defines the site where LC3 (homologue of yeast Atg8) is conjugated to phosphatidylethanolamine (PE), an essential process for autophagy, by recruitment of an Atg3-LC3 intermediate to a source membrane of an autophagosome[10,11]. In addition, Atg16L1 has seven WD40 repeats at the carboxy terminus, which are absent in yeast Atg16 (ref. 10). Recent genome-wide association studies identified Atg16L1 as a candidate gene responsible for susceptibility to Crohn's disease[6,7]. However, the importance of Atg16L1 in autophagy and its role in inflammation have not been fully understood. Hence, we generated Atg16L1 mutant mice and examined the function of Atg16L1 in autophagosome formation as well as in the regulation of immune responses.

Atg16L1 mutant mice express deleted forms of Atg16L1 protein lacking the entire coiled-coil domain (Fig. 1a, b, and Supplementary Fig. 1a–c). However, such aberrant proteins do not act as dominant-negative molecules, because ectopic expression of truncated Atg16L1 protein lacking the coiled-coil domain (ΔCCD) in wild-type mouse embryonic fibroblasts (MEFs) did not interfere with autophagy (Supplementary Fig. 2a, b). Most Atg16L1-deficient mice died within 1 day of delivery, indicating that Atg16L1 is required for survival during neonatal starvation (Supplementary Fig. 1d, e). This phenotype is similar to that observed in Atg5- or Atg7-deficient mice[12,13]. Although Atg16L1 associates with Atg12-Atg5, Atg16L1 was dispensable for Atg12 conjugation to Atg5 (Fig. 1b). On the other hand, Atg16L1 was required for LC3 conjugation to PE (Fig. 1b). In Atg16L1-deficient MEFs, formation of the high molecular weight protein complex was disrupted and Atg12-Atg5 puncta were hardly observed (Fig. 1c, d, and Supplementary Fig. 3, 4a). On the other hand, GFP-Atg5 free from Atg12-conjugation formed puncta in Atg7-deficient MEFs or Atg5-deficient MEFs complemented with GFP-Atg5^{K130R}, although these puncta did not colocalize with LC3 (Fig. 1c, d, Supplementary Figs 4b, 5, data not shown). Formation of autophagosomes under the starved condition was not observed in Atg16L1-deficient MEFs, resulting in a decrease in the bulk degradation of long-lived proteins and the accumulation of p62/SQSTM1 (Fig. 1b–f). These results indicated that Atg16L1 is essentially required for autophagy by regulating the localization of the Atg12-Atg5 conjugate.

[1]Laboratory of Host Defense, [2]Laboratory of Gastrointestinal Immunology, WPI Immunology Frontier Research Center, Osaka University, 3-1 Yamada-oka, Suita, Osaka 565-0871, Japan. [3]Department of Host Defense, [4]Department of Cellular Regulation, Research Institute for Microbial Diseases, Osaka University, 3-1 Yamada-oka, Suita, Osaka 565-0871, Japan. [5]AIDS Research Center, National Institute of Infectious Diseases, Toyama 1-23-1, Shinjuku-ku, Tokyo 162-8640, Japan. [6]Laboratory of Frontier Science, Tokyo Metropolitan Institute of Medical Science, Bunkyo-ku, Tokyo 113-8613, Japan. [7]Department of Biochemistry, Juntendo University School of Medicine, 2-1-1 Hongo Bunkyo-ku, Tokyo 113-8421, Japan. [8]PRESTO, Japan Science and Technology Corporation, Kawaguchi, Saitama 332-0012, Japan. [9]Department of Pathology, Hyogo College of Medicine, 1-1 Mukogawa-cho, Nishinomiya, Hyogo 663-8501, Japan. [10]CREST, Japan Science and Technology Agency, 4-1-8 Honcho, Kawaguchi, Saitama 332-0012, Japan.
*These authors contributed equally to this work.

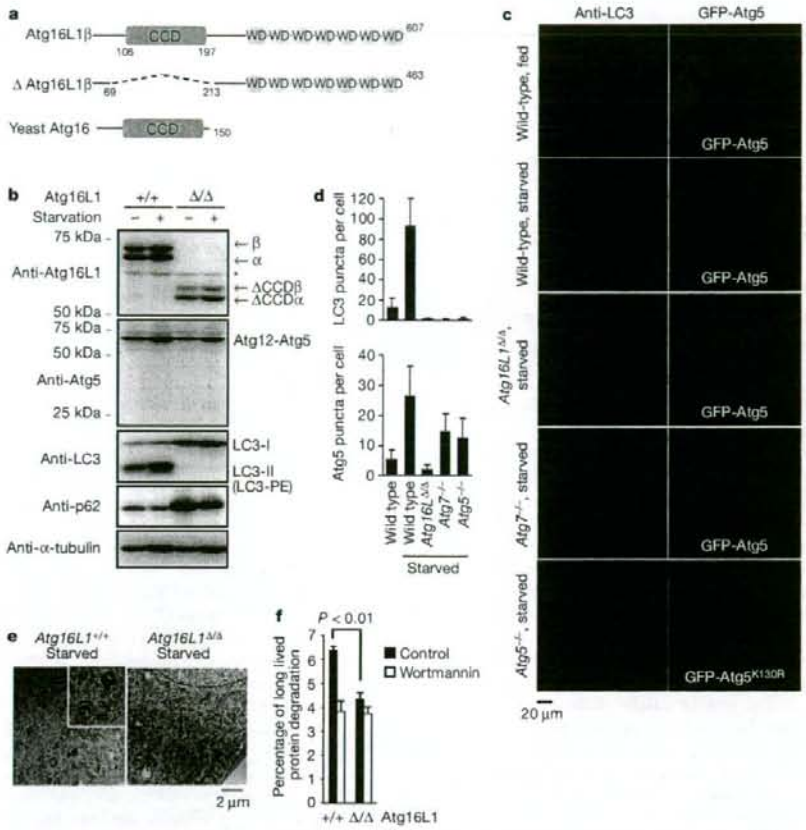

Figure 1 | Atg16L1 is essential for autophagy. a, Schematic structure of wild-type or truncated (Δ) Atg16L1 protein. CCD, Coiled-coil domain; WD, WD40 domain. Here and below, suffix α or β indicates isoform α or β. **b–d**, MEFs were cultured in nutrient-rich medium (fed) or Hanks' buffer (starved) for 1 h. Total cell lysates were prepared, and blotted with the indicated antibodies (**b**). α, β, indicate Atg16L1 isoform α, β; ΔCCD indicates Atg16L1ΔCCD; asterisk indicates a non-specific band. *Atg16L1*$^{\Delta/\Delta}$ indicates mice expressing ΔAtg16L1. The number of endogenous LC3 or GFP-Atg5 dots was counted (**c, d**). The results shown are mean + s.d. ($n > 20$). **e**, Electron micrograph of starved MEFs. **f**, Degradation of long-lived proteins in MEFs. Wortmannin is an autophagy inhibitor. The results shown are mean + s.d. Statistical significance (*P* value) was determined by the Student's *t*-test.

Although the involvement of autophagic machinery in the Toll-like receptor (TLR)-mediated antiviral response and phagocytosis have been reported[14,15], it is still unclear whether autophagy controls TLR-mediated inflammatory responses. We examined the role of Atg16L1 in the production of inflammatory cytokines, such as TNFα, IL-6 and IL-1β, in response to lipopolysaccharide (LPS), a major component of bacterial endotoxin[8]. Although both messenger RNA expression and production of TNFα, IL-6 and IFN-β were almost normal in Atg16L1-deficient fetal liver-derived macrophages, IL-1β production was highly elevated compared with that in wild-type macrophages (Fig. 2a, Supplementary Fig. 6). IL-1β mRNA synthesis was not impaired in Atg16L1-deficient macrophages, indicating that IL-1β production is enhanced at the post-transcriptional level in Atg16L1-deficient macrophages (Supplementary Fig. 6). Synthetic lipid A, an active component of LPS, also potently induced IL-1β production in Atg16L1-deficient cells (Fig. 2b). On the other hand, ectopic expression of the Atg16L1 protein lacking coiled-coil domain (ΔCCD) in RAW264.7 cells did not affect LPS-induced IL-1β production (Supplementary Fig. 2c, d). These results indicated that Atg16L1-deficiency is responsible for the elevated production of IL-1β.

We next generated chimaeric mice by transplantation of fetal liver cells into lethally irradiated CD45.1 mice to examine IL-1β production in other types of macrophage (Supplementary Fig. 7a–c). Following stimulation with LPS, peritoneal and bone-marrow macrophages deficient in Atg16L1 showed enhanced IL-1β production compared with wild-type macrophages (Supplementary Fig. 7d, e). Non-invasive Gram-negative bacteria, such as *Escherichia coli*, *Enterobacter aerogenes* and *Klebsiella pneumonia*, which are habitants in the commensal flora, also potently induced IL-1β production in Atg16L1-deficient cells (Supplementary Fig. 8a). On the other hand, the production of IL-1β and apoptosis induced by *Salmonella typhimurium*, an invasive Gram-negative bacterium, is almost normal in Atg16L1-deficient macrophages (Fig. 2c, Supplementary Fig. 9c). We also found that Atg16L1-deficient macrophages produced a high amount of IL-1β following stimulation by ATP or monosodium urate (MSU), an activator of the Nalp3 inflammasome[16,17] (Fig. 2c). Atg16L1-deficient macrophages normally produced inflammatory cytokine in response to muramyldipeptide, a ligand for NOD2 (ref. 16), indicating that Atg16L1 is not involved in signalling downstream of NOD2, whose de-regulation is also implicated in Crohn's disease[18] (Supplementary Fig. 10).

The expression levels of immature IL-1β protein following LPS stimulation in Atg16L1-deficient macrophages were almost comparable to those in wild-type cells, indicating an abnormality of post-translational regulation (Fig. 2d). Cleaved caspase-1, an activated

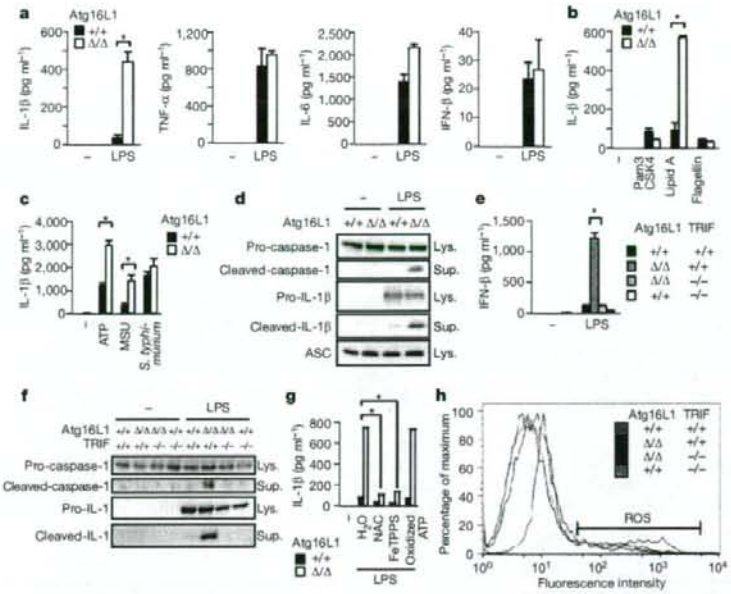

Figure 2 | Elevated endotoxin-induced IL-1β production from Atg16L1-deficient macrophages. **a**, Cytokine production from macrophages stimulated with LPS (100 ng ml^{-1}) for 24 h. Statistical significance was determined by the Student's *t*-test. $^*P < 0.01$. **b**, IL-1β production from macrophages stimulated with indicated ligands. **c**, IL-1β production from LPS-primed macrophages infected with *S. typhimurium* (multiplicity of infection, m.o.i., 1), or stimulated with ATP or MSU for 1 h. **d**, Expression levels of caspase-1 and IL-1β in macrophages. Lys., cell lysates; Sup., culture supernatants. **e**, LPS-induced production of IL-1β from macrophages with the indicated phenotype. **f**, Expression levels of caspase-1 and IL-1β in macrophages treated as in **e**. **g**, Effect of the ROS scavenger FeTPPS (25 μM), N-acetyl-L-cysteine (NAC; 25 mM) or P2X7 receptor antagonist oxidized ATP (250 μM) on IL-1β production. **h**, ROS in LPS-stimulated macrophages were detected by CM-H_2DCFDA staining.

form that mediates processing of IL-1β and apoptosis[16,17], was detected in the culture supernatants of Atg16L1-deficient macrophages following LPS stimulation, and was responsible for the production of IL-1β and the induction of apoptosis (Fig. 2d, Supplementary Figs 9a, b, 11). IL-18 production, which is regulated by caspase-1-mediated cleavage[17], was also enhanced in response to LPS in Atg16L1-deficient macrophages (Supplementary Fig. 12). Recent studies have disclosed that NF-κB and p38 signalling pathways regulate the activation of caspase-1 and the induction of cell death in macrophages stimulated with LPS[18,19]. However, activation of NF-κB, p38 and IRF-3 signalling pathways by LPS was comparable between wild-type and Atg16L1-deficient macrophages (Supplementary Fig. 13). Among TLR family members, TLR2, TLR4 and TLR5 recognize bacterial components and play important roles in the anti-bacterial response[8]. Importantly, TLR4 ligand, but not ligands for TLR2 or TLR5, induced potent IL-1β production from Atg16L1-deficient macrophages (Fig. 2b, Supplementary Fig. 14). Enhancement of IL-1β production in Atg16L1-deficient macrophages was also induced by ligands for the viral nucleotide-sensing TLRs, TLR3, TLR7 and TLR9, although the production induced by these ligands was lower than that induced by LPS (Supplementary Fig. 14).

These findings prompted us to assess the involvement of the TRIF/IFN signalling, which is strongly triggered by the engagement of TLR4 in macrophages[8] and regulates apoptosis[18]. Consistent with this hypothesis, Atg16L1/TRIF double-deficient macrophages failed

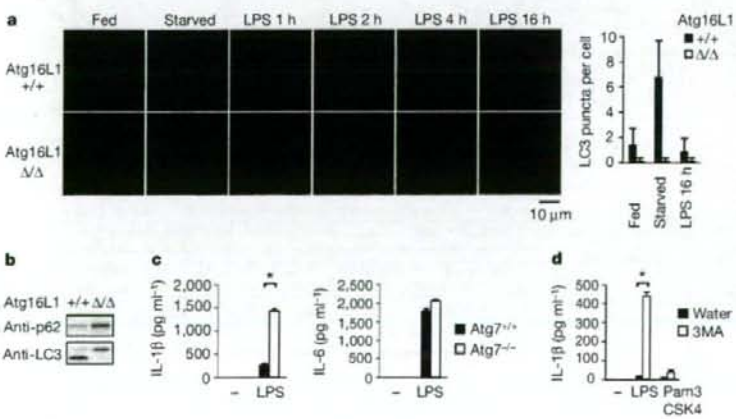

Figure 3 | Disruption of basal autophagy enhances LPS-induced IL-1β production. **a**, Macrophages were stimulated with LPS (100 ng ml^{-1}) for the indicated time period. The number of endogenous LC3 dots within each cell was counted. The results shown are mean + s.d. ($n > 100$). **b**, Expression levels of p62 and LC3 in macrophages. **c**, IL-1β and IL-6 production by wild-type or Atg7-deficient macrophages stimulated with LPS. Statistical significance was determined by the Student's *t*-test. $^*P < 0.01$. **d**, Macrophages were pre-treated with or without 10 mM 3MA and then stimulated with the indicated ligands.

to produce IL-1β due to a lack of caspase-1 activation in response to LPS (Fig. 2e, f). The simultaneous stimulation of Atg16L1-deficient macrophages with IFN-β or IFN-γ enhanced IL-1β production and apoptosis induced by TLR2 ligand (Supplementary Figs 9d, 15a). Recent studies have disclosed that K^+-efflux and reactive oxygen species (ROS), especially peroxynitrate, play important roles in the production of IL-1β induced by ATP, MSU and asbestos[16,17,20,21]. Similarly, the enhanced IL-1β production from Atg16L1-deficient macrophages required K^+-efflux and ROS generation (Fig. 2g, Supplementary Figs 15b, 16). The level of ROS in Atg16L1-deficient macrophages was higher than that in Atg16L1/TRIF double-deficient or wild-type macrophages following LPS stimulation (Fig. 2h). Oxidized ATP, an antagonist for the P2X7 receptor, did not inhibit LPS-induced IL-1β production, indicating that extracellular ATP is not involved in its production (Fig. 2g). These results indicate that loss of Atg16L1 in macrophages causes aberrant LPS-induced IL-1β production in a TRIF-dependent manner. ROS might be accumulated in Atg16L1-deficient macrophages undergoing apoptosis and trigger caspase-1 activation following LPS stimulation.

The involvement of TLR signalling in the induction of autophagy has been recently reported[22,23]. Therefore we examined if stimulation of TLR4 or other TLRs induces puncta formation by endogenous LC3. In contrast to previous reports, LPS stimulation did not increase the number of LC3 puncta in primary macrophages, although nutrient deprivation induced the formation of autophagosomes (Fig. 3a, Supplementary Fig. 17a–c). Stimulation by other ligands for TLRs also failed to increase the number of puncta of endogenous LC3 in these macrophages (Supplementary Fig. 17b, d, e). Co-incubation with non-invasive bacteria did not increase the number of autophagosomes in macrophages (Supplementary Fig. 8b). On the other hand, infection with *S. typhimurium* resulted in Atg16L1-dependent formation of bacteria autophagosomes, even in the absence of both MyD88 and TRIF, essential adaptor molecules for TLR signalling pathways[8,9] (Supplementary Fig. 18a, b). These results indicated that TLR signalling is not associated with the formation of autophagosomes in primary macrophages.

Increasing evidence has revealed that basal autophagy plays critical roles under both physiological and pathological conditions, including neurodegeneration, hepatic dysfunction and the immune response[13,24–26]. In Atg16L1-deficient macrophages, autophagosomes were hardly detected and p62/SQSTM1 protein was accumulated under nutrient-rich conditions, indicating that basal autophagy is almost completely inhibited (Fig. 3a, b). Atg7-deficient macrophages also produced high levels of IL-1β in response to LPS, but produced normal levels of IL-6 (Fig. 3c). A chemical inhibitor of autophagy, 3-methyladenine (3MA), significantly enhanced production of IL-1β from wild-type peritoneal macrophages induced by stimulation with LPS, but not with ligand for TLR2 (Fig. 3d). Macrophages treated with 3MA underwent apoptosis following LPS stimulation (Supplementary Fig. 9e). Further, transient expression of inactive mutant of Atg4B, which inhibits the LC3 lipidation, enhanced LPS-induced IL-1β production in RAW264.7 cells (Supplementary Fig. 19a, b). These results indicate that inhibition of basal autophagy induces IL-1β overproduction.

Aberrant expression of inflammatory cytokines, including IL-1β and IL-18, has been shown to be involved in the development of colitis[27,28], and recent studies have reported that Atg16L1 is a candidate susceptibility gene for Crohn's disease[6,7]. Under specific pathogen-free conditions, Atg16L1-deficient chimaeric mice did not develop spontaneous colitis, and the colons of newborn Atg16L1-deficient mice were not inflamed (Supplementary Fig. 20a, b). The number of bacteria in the faeces of wild-type or Atg16L1-deficient chimaeric mice was almost same, and no bacteria were detected in spleen (Supplementary Fig. 20c, d). The number of $CD4^+Foxp3^+$ regulatory T cells, which suppress the inflammatory response and are required for immune homeostasis[29], was almost normal in the spleens and mesenteric lymph nodes of Atg16L1-deficient chimaeric mice (Supplementary Fig. 21a, b). We next assessed if Atg16L1-deficiency exacerbates inflammation in a dextran sulphate sodium (DSS)-induced experimental model of colitis. Strikingly, all chimaeric mice with Atg16L1-deficient haematopoietic cells died together with severe body weight loss following seven days of DSS exposure, whereas all chimaeric mice expressing wild-type Atg16L1 survived (Fig. 4a, b). Histological analyses revealed much severer inflammation in the distal colons of Atg16L1-deficient mice than in wild-type controls, with larger areas of ulceration and increased infiltration of lymphocytes

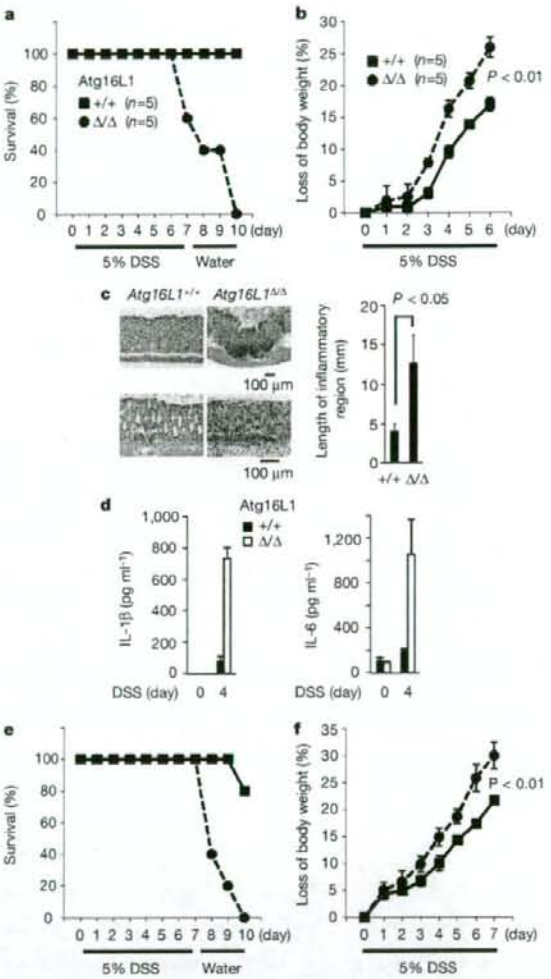

Figure 4 | Severe DSS-induced colitis in Atg16L1-deficient chimaeric mice. **a**, **b**, Fetal liver chimaeric mice were given 5% DSS in drinking water for 7 days. The survival (**a**) and weight loss (**b**) of each mouse genotype were plotted. The results shown are mean ± s.d. Statistical significance was determined by the Student's *t*-test. **c**, Typical distal colon appearance 6 days after the initiation of DSS administration. The results shown are mean ± s.d. ($n = 3$, each group). **d**, Expression levels of IL-1β and IL-18 in serum ($n = 5$, each group). **e**, **f**, Atg16L1-deficient chimaeric mice given 5% DSS in drinking water were intraperitoneally injected with both anti-IL-1β and anti-IL-18 neutralizing antibodies (squares; $n = 5$) or isotype control IgG (circles; $n = 5$) at days 1, 3, 5 and 7. The survival (**e**) and weight loss (**f**) of each mouse genotype were plotted.

(Fig. 4c). The levels of the proinflammatory cytokines IL-1β and IL-18 were significantly elevated in the sera of DSS-treated Atg16L1-deficient chimaeric mice relative to the levels in wild-type counterparts (Fig. 4d). Mortality and loss of body weight after DSS-exposure in Atg16L1-deficient chimaeric mice were improved by the injection of neutralizing antibodies for IL-1β and IL-18, showing the involvement of excessive production of these cytokines in the development of severe colitis (Fig. 4e, f). Administration of 3MA increased the level of IL-1β in serum and worsened the survival rate of mice treated with DSS, suggesting that autophagy protects mice from massive inflammation during colitis (Supplementary Fig. 22).

Our present study highlights a novel role for autophagy in the regulation of the inflammatory immune response. Autophagy controls inflammasome activation and limits production of the inflammatory cytokines IL-1β and IL-18. Given the importance of elevated expression of IL-1β and IL-18 caused by Atg16L1 deficiency in the pathology of chemical-induced colitis, it would be of interest to examine the involvement of autophagy in the pathogenesis of inflammatory bowel diseases such as Crohn's disease.

METHODS SUMMARY

Mice, reagents, cells and plasmids. Details are given in Methods.

Preparation of macrophages. E15.5 fetal liver stem cells from wild-type or Atg16L1-deficient littermates were cultured in the presence of GM-CSF (10 ng ml^{-1}) for 7 days to generate fetal liver macrophages. Unattached cells were removed on days 2, 4 and 6. Unless otherwise noted, fetal liver macrophages were used in the experiments. Bone-marrow-derived and peritoneal macrophages were prepared as described[9].

Histopathological analysis. The colon was removed and fixed with 4% PFA. The paraffin sections were stained with haematoxylin and eosin (H&E), and histologically analysed.

RT–PCR, immunoblotting, ELISA. Details of RT–PCR procedures are given in Methods. Immunoblotting was performed as described[11], and the experiments were repeated at least twice. The level of cytokine production was measured by ELISA according to the manufacturer's instructions. The results shown are means ± s.d. from three separate samples. The experiments were repeated at least three times.

Fluorescence microscopy analysis. Cells cultured on coverslips were fixed with 3% paraformaldehyde, and subjected to immunocytochemistry[11]. Samples were examined under a fluorescence laser scanning confocal FV1000 microscope (Olympus).

Detection of ROS. Macrophages were stimulated with LPS for 22 h, and then stained with CM-H_2DCFDA (10 μM; Molecular Probes), a fluorescent indicator for ROS, for 2 h. The level of fluorescence was determined by flow cytometry. The experiments were repeated at least three times.

Gel filtration, electron microscopy analysis, bulk protein degradation assay. Gel filtration analysis was performed as described[11]; electron microscopy analysis was performed as described[10]; details on the bulk protein degradation assay are given in Methods.

Full Methods and any associated references are available in the online version of the paper at www.nature.com/nature.

Received 7 August; accepted 26 August 2008.
Published online 5 October 2008.

1. Liu, Y. C., Penninger, J. & Karin, M. Immunity by ubiquitylation: A reversible process of modification. *Nature Rev. Immunol.* **5**, 941–952 (2005).
2. Wang, Y. *et al.* Lysosome-associated small Rab GTPase Rab7b negatively regulates TLR4 signaling in macrophages by promoting lysosomal degradation of TLR4. *Blood* **110**, 962–971 (2007).
3. Ohsumi, Y. Molecular dissection of autophagy: Two ubiquitin-like systems. *Nature Rev. Mol. Cell Biol.* **2**, 211–216 (2001).
4. Mizushima, N., Levine, B., Cuervo, A. M. & Klionsky, D. J. Autophagy fights disease through cellular self-digestion. *Nature* **451**, 1069–1075 (2008).
5. Levine, B. & Deretic, V. Unveiling the roles of autophagy in innate and adaptive immunity. *Nature Rev. Immunol.* **7**, 767–777 (2007).
6. Hampe, J. *et al.* A genome-wide association scan of nonsynonymous SNPs identifies a susceptibility variant for Crohn disease in ATG16L1. *Nature Genet.* **39**, 207–211 (2007).
7. Rioux, J. D. *et al.* Genome-wide association study identifies new susceptibility loci for Crohn disease and implicates autophagy in disease pathogenesis. *Nature Genet.* **39**, 596–604 (2007).
8. Akira, S., Uematsu, S. & Takeuchi, O. Pathogen recognition and innate immunity. *Cell* **124**, 783–801 (2006).
9. Yamamoto, M. *et al.* Role of adaptor TRIF in the MyD88-independent toll-like receptor signaling pathway. *Science* **301**, 640–643 (2003).
10. Mizushima, N. *et al.* Mouse Apg16L, a novel WD-repeat protein, targets to the autophagic isolation membrane with the Apg12-Apg5 conjugate. *J. Cell Sci.* **116**, 1679–1688 (2003).
11. Fujita, N., Itoh, T., Fukuda, M., Noda, T. & Yoshimori, T. The Atg16L complex specifies the site of LC3 lipidation for membrane biogenesis in autophagy. *Mol. Biol. Cell* **19**, 2092–2100 (2008).
12. Kuma, A. *et al.* The role of autophagy during the early neonatal starvation period. *Nature* **432**, 1032–1036 (2004).
13. Komatsu, M. *et al.* Impairment of starvation-induced and constitutive autophagy in Atg7-deficient mice. *J. Cell Biol.* **169**, 425–434 (2005).
14. Lee, H. K., Lund, J. M., Ramanathan, B., Mizushima, N. & Iwasaki, A. Autophagy-dependent viral recognition by plasmacytoid dendritic cells. *Science* **315**, 1398–1401 (2007).
15. Sanjuan, M. A. *et al.* Toll-like receptor signalling in macrophages links the autophagy pathway to phagocytosis. *Nature* **450**, 1253–1257 (2007).
16. Kanneganti, T. D., Lamkanfi, M. & Núñez, G. Intracellular NOD-like receptors in host defense and disease. *Immunity* **27**, 549–559 (2007).
17. Pétrilli, V., Dostert, C., Muruve, D. A. & Tschopp, J. The inflammasome: A danger sensing complex triggering innate immunity. *Curr. Opin. Immunol.* **19**, 615–622 (2007).
18. Hsu, L. C. *et al.* The protein kinase PKR is required for macrophage apoptosis after activation of Toll-like receptor 4. *Nature* **428**, 341–345 (2004).
19. Greten, F. R. *et al.* NF-κB is a negative regulator of IL-1β secretion as revealed by genetic and pharmacological inhibition of IKKβ. *Cell* **130**, 918–931 (2007).
20. Dostert, C. *et al.* Innate immune activation through Nalp3 inflammasome sensing of asbestos and silica. *Science* **320**, 674–677 (2008).
21. Hewinson, J., Moore, S. F., Glover, C., Watts, A. G. & MacKenzie, A. B. A key role for redox signaling in rapid P2X7 receptor-induced IL-1beta processing in human monocytes. *J. Immunol.* **180**, 8410–8420 (2008).
22. Xu, Y. *et al.* Toll-like receptor 4 is a sensor for autophagy associated with innate immunity. *Immunity* **27**, 135–144 (2007).
23. Delgado, M. A., Elmaoued, R. A., Davis, A. S., Kyei, G. & Deretic, V. Toll-like receptors control autophagy. *EMBO J.* **27**, 1110–1121 (2008).
24. Hara, T. *et al.* Suppression of basal autophagy in neural cells causes neurodegenerative disease in mice. *Nature* **441**, 885–889 (2006).
25. Komatsu, M. *et al.* Homeostatic levels of p62 control cytoplasmic inclusion body formation in autophagy-deficient mice. *Cell* **131**, 1149–1163 (2007).
26. Paludan, C. *et al.* Endogenous MHC class II processing of a viral nuclear antigen after autophagy. *Science* **307**, 593–596 (2005).
27. Maeda, S. *et al.* Nod2 mutation in Crohn's disease potentiates NF-κB activity and IL-1β processing. *Science* **307**, 737–738 (2005).
28. Ishikura, T. *et al.* Interleukin-18 overproduction exacerbates the development of colitis with markedly infiltrated macrophages in interleukin-18 transgenic mice. *J. Gastroenterol. Hepatol.* **18**, 960–969 (2003).
29. Izcue, A., Coombes, J. L. & Powrie, F. Regulatory T cells suppress systemic and mucosal immune activation to control intestinal inflammation. *Immunol. Rev.* **212**, 256–271 (2006).
30. Nakagawa, I. *et al.* Autophagy defends cells against invading group A Streptococcus. *Science* **306**, 1037–1040 (2004).

Supplementary Information is linked to the online version of the paper at www.nature.com/nature.

Acknowledgements We are grateful to T. Kitamura, S. Yamaoka and N. Mizushima for providing materials. We thank K. J. Ishii, M. Yamamoto and members of the Laboratory of Host Defense for discussions; Y. Fujiwara, M. Shiokawa, R. Nakayama and N. Kitagaki for technical assistance; and M. Hashimoto and E. Kamada for secretarial assistance. This work was in part supported by grants from NIH (AI070167) and the Ministry of Health, Labour and Welfare of Japan, and by Grant-in-Aid for Specially Promoted Research from the Ministry of Education, Culture, Sports, Science and Technology of Japan.

Author Contributions T.S. generated the Atg16L1-deficient mice and performed the immunological experiments. N.F. performed the cell biology experiments. N.Y. generated the retroviral vector. M.K. and K.T. generated the Atg7-deficient mice. T.T. performed histological analysis of mice. M.H.J., S.U., B.-G.Y., T.S., H.O., T.N., T.K. and O.T. helped with experiments. T.Y. designed the cell biology research. S.A. supervised the overall research project.

Author Information Reprints and permissions information is available at www.nature.com/reprints. Correspondence and requests for materials should be addressed to S.A. (akira@biken.osaka-u.ac.jp).

METHODS

Generation of Atg16L1-deficient mice. The fragment of the Atg16L1 gene was isolated from genomic DNA extracted from wild-type ES cells by PCR. A targeting vector was constructed by replacing exons 3, 4 and 5 of Atg16L1 with a neomycin-resistance gene cassette (neo), and a herpes simplex virus thymidine kinase driven by PGK promoter was inserted into the genomic fragment for negative selection. After the targeting vector was transfected into ES cells, G418 and gancyclovir doubly resistant colonies were selected and screened by PCR and Southern blotting. Homologous recombinants were micro-injected into C57BL/6 female mice, and heterozygous F1 progenies were intercrossed in order to obtain Atg16L1-deficient (Δ/Δ) mice. The Atg16L1-deficient mice used were on a 129Sv × C57BL/6 background.

For the generation of fetal liver chimaeric mice, fetal liver cells were harvested at E15.5 and injected into lethally irradiated CD45.1 or C57BL6J mice. Chimaeric mice were given antibiotics in drinking water for 2 months. The mice were analysed at least 3 months after reconstitution.

Mice were maintained in our animal facility and treated in accordance with the guidelines of Osaka University.

Reagents, mice and cells. Anti-IL-1β antibodies, recombinant mouse IFN-γ, ELISA kits for mouse IL-1β, human IL-1β, mouse IL-6 and mouse TNFα, were purchased from R&D Systems. Recombinant mouse IFN-β and the ELISA kit for mouse IFN-β were purchased from PBL InterferonSource. Anti-LC3 and anti-IL-18 antibodies and the ELISA kit for IL-18 were purchased from MBL International. GM-CSF and M-CSF were purchased from Peprotech. Anti-p62/SQSTM1 antibody was purchased from BIOMOL International. Anti-Atg12, anti-phospho-IRF3, anti-phospho-p38 and anti-phospho-ERK antibodies were purchased from Cell Signaling Technology. Anti-IκBα, anti-ERK and caspase-1 p10 were purchased from Santa Cruz Biotechnology. YVAD-fmk, wortmannin and FeTPPS were purchased from Calbiochem. ATP, oxidized ATP, LPS from *Salmonella minnesota* Re 595, 3-methyadenine, muramyl dipeptide and anti-α-tubulin antibody were purchased from Sigma. Lipid A was purchased from Peptide Institute. Flagellin was purchased from Invivogen. Uric acid crystals were purchased from Alexis. N-acetyl-L-cysteine was purchased from Nacalai Tesque. Poly(I)·poly(C) was purchased from GE Healthcare. R-848 was kindly provided by the Pharmaceuticals and Biotechnology Laboratory Japan Energy Corporation. CpG oligodeoxynucleotides (ODN1668) were synthesized at Hokkaido System Science Co. Anti-Atg16L1and anti-Atg5 antibodies were kindly donated by N. Mizushima (Tokyo Medical and Dental University).

K. pneumonia and *E. aerogenes* were kindly donated by the Research Institute of Microbial Disease, Osaka University. *E. coli* (DH5α) was purchased from TOYOBO. *Salmonella enteritica serovar typhimurium* (SR-11 × 3181) was provided by the Kitasato Institute for Life Science. Mice deficient in MyD88, TRIF or Atg7 were described previously[9,13]. Atg5-deficient MEFs and Plat-E cells were kindly donated by N. Mizushima and T. Kitamura (University of Tokyo), respectively. RAW264.7 cells were purchased from ATCC.

Plasmids. The retroviral expression constructs pMRX-ires-puro, pMRX-ires-bsr and pMRX-ires-EGFP (donated by S. Yamaoka) were derivatives of pMX (donated by T. Kitamura). Complementary DNA encoding human IL-1β was inserted into pMRX-ires-EGFP, generating pMRX-ires-IL-1β. Complementary DNA encoding Atg16L1 lacking in coiled-coil domain (Atg16L1 ΔCCDβ) was inserted into pMRX-ires-puro, generating pMRX-Atg16L1 ΔCCDβ-ires-puro. Complementary DNA encoding the GFP-Atg5 chimaeric protein was inserted into pMRX-ires-bsr, generating pMRX-GFP-Atg5-ires-bsr. Construction and inhibitory function details of pStrawberry-Atg4^{C74A} are described elsewhere[31].

RT–PCR. Total RNA was isolated using RNAeasy Mini kits (Qiagen) according to the manufacturer's instructions. Reverse transcription was performed using ReverTra Ace (TOYOBO) according to the manufacturer's instructions. For quantitative PCR, cDNA fragments were amplified by RealTime PCR Master Mix (TOYOBO) according to the manufacturer's instructions. Fluorescence from the Taqman probe for each cytokine was detected by a 7500 Real-Time PCR System (Applied Biosystems). To determine the relative induction of cytokine mRNA in response to LPS stimulation, the mRNA expression level of each cytokine was normalized to the expression level of 18S RNA. The experiments were repeated at least twice. The results were reproducible.

The primer pairs used in Supplementary Fig. 1 are as follows. Primer pair A (exon 1-2), 5′-GTTCGGCATGTCGTCGGGCCTG-3′ and 5′-ATTTCATGCC-TATTTGGCATGTCATGC-3′. Primer pair B (exon 6-7), 5′-GTCAAGCACG-GCTGCAGAAGGAGCTTG-3′ and 5′-GTAGCTGCTCTGCTGACAGCTCGG-3′. Primer pair C (exon 1-5), 5′-GTTCGGCATGTCGTCGGGCCTGN-3′ and 5′-GACCAGTTCCTGGTTCTCCTCAGTAG-3′. Primer pair D (exon 5-7), 5′-CGCCTCAATGCAGAGAATGAGAAGGAC-3′ and 5′-GTAGCTGCTCTGCT-GACAGCTCGG-3′. Primer pair E (exon 1-6), 5′-GTTCGGCATGTCGTCG-GGCCTG-3′ and 5′-CAAGCTCCTTCTGCAGCCGTGCTTGAC-3′.

Bulk protein degradation assay. Cells were exchanged into labelling medium containing ^{14}C-valine (1.5 μCi ml^{-1}) and incubated overnight. Cells were exchanged into chase medium (DMEM supplemented with 10% FBS and 10 mM unlabelled valine) and further incubated for 4 h to remove the contribution of short-lived proteins. After the chase period, cells were exchanged into HBSS containing 10 mM valine to induce autophagy. After a 2 h incubation, the media were collected and the trichloroacetic acid (TCA)-soluble fraction was analysed by scintillation counting. Cells were lysed in ice-cold RIPA buffer and the TCA-insoluble fraction was isolated and analysed by scintillation counting. To determine the rate of long-lived protein degradation, the count in the TCA-soluble fraction in the medium was divided by the equivalent TCA-insoluble count in the cell.

Detection of apoptosis. The appearance of mono/oligo-nucleosomes, markers for apoptosis, was detected by Cell Death Detection ELISA^{PLUS} (Roche). Chromatin condensation in apoptotic nuclei was detected using an ApoStrand ELISA Apoptosis Detection Kit (Biomol). The experiments were repeated twice, and the results were reproducible.

Determination of bacteria colony forming units (c.f.u.s). Levels of c.f.u.s in freshly isolated faeces or spleen were determined by homogenization of material in PBS/0.01% Triton X-100 followed by serial dilution plating on non-selective Luria-Bertani agar.

31. Fujita, N. *et al.* An Atg4B mutant hampers the lipidation of LC3 paralogues and causes defects in autophagosome closure. *Mol. Biol. Cell* advance online publication, doi:10.1091/mbc.E08-03-0312 (3 September 2008).

Fluorophore Labeling Enables Imaging and Evaluation of Specific CXCR4−Ligand Interaction at the Cell Membrane for Fluorescence-Based Screening

Wataru Nomura,[†] Yasuaki Tanabe,[†] Hiroshi Tsutsumi,[†] Tomohiro Tanaka,[†] Kenji Ohba,[‡] Naoki Yamamoto,[‡] and Hirokazu Tamamura*[,†]

Institute of Biomaterials and Bioengineering, Tokyo Medical and Dental University, Chiyoda-ku, Tokyo 101-0062, Japan, and AIDS Research Center, National Institute of Infectious Diseases, Shinjuku-ku, Tokyo 162-8640, Japan. Received May 24, 2008; Revised Manuscript Received July 23, 2008

Development of CXCR4-specific ligands is an important issue in chemotherapy of HIV infection, cancer metastasis, and rheumatoid arthritis, and numerous potential ligands have been developed to date. However, it is difficult to assess their binding mode and specificity because of uncertainties in the structure of the CXCR4−ligand complexes. To address this problem, we have synthesized fluorophore labeled Ac-TZ14011, which is derived from T140, a powerful CXCR4 antagonist. Binding of Ac-TZ14011 to CXCR4 on the cell membrane was observed by fluorescence microscope, and analysis of the binding data produced IC_{50} values of several ligands comparable to those obtained in RI-based assays. This fluorescence-based assay is applicable to explore new pharmacophores of CXCR4-specific ligands with high-throughput screening and also to screening of the other GPCR binding ligands.

The interaction of CXCR4 with ligands causes diverse effects on cellular functions such as metastasis of progenitor cells (*1*−*3*), and a major role of CXCR4 is as the receptor of the chemokine, CXCL12. The interaction of CXCL12 with CXCR4 has been shown to be correlated with cancer progression (*4*) and $CD4^+$ T cell accumulation in the rheumatoid arthritis synovium (*5*). CXCR4 is also known as the second receptor of X4-type HIV-1 (*6*), and numerous ligands for CXCR4 derived from natural and synthetic compounds have been identified as inhibitors of HIV infection and cancer metastasis. [^{125}I]-CXCL12 has been utilized as a competitor in the assays to evaluate the CXCR4-binding activity of synthetic compounds such as T140 (*7*), its derivatives (*8*), KRH-1636 (*9*), and AMD3100 (*10*). Experimental methods utilizing radioisotopes (RI[1]) have advantages in the high resolution of the assays. Recently, molecular probes and fluorescent labeling, an emergent technology in chemical biology, have proved to be very useful for the evaluation in vivo of the functions of proteins and of the biological effect of changing concentrations of Ca^{2+} (*11*), Zn^{2+} (*12*), and NO (*13*), enzyme activity (*14*), and protein phosphorylation (*15*) in cells. Moreover, imaging of living cells by fluorescent probes can be utilized to estimate the accuracy of binding assays under statistically identical conditions. This article describes the synthesis and use of fluorophore labeled Ac-TZ14011 to analyze the CXCR4 binding of ligands at the cell membrane and to determine the IC_{50} values of ligands.

Ac-TZ14011, a derivative of T140 optimized for CXCR4 binding and stability in vivo by functional group substitutions, was synthesized as described previously (*16*, *17*). The D-lysine at position 8 was selectively labeled with TAMRA or fluorescein (Figure 1). A hexamethylene group was incorporated into the TAMRA or fluorescein derivative to maintain an appropriate distance between T140 residues and the fluorophore. Residues critical to the CXCR4 binding activity of TZ14011 are Arg2, Nal3, Tyr5, and Arg14, and were assessed by screening of amino acid substitution of T140 (*16*). On the basis of the previously determined interaction between Ac-TZ14011 and CXCR4 (*18*), the fluorophores labeled at D-lysine 8 were assumed not to inhibit binding of fluorescent-Ac-TZ14011 to CXCR4. To investigate if fluorescent labeled Ac-TZ14011 maintains binding activity against CXCR4, the IC_{50} values of peptides were estimated by competitive assays against [^{125}I]-CXCL12 binding. In this assay, the IC_{50} of T140 was 3.7 nM. The IC_{50} values for fluorescein- or TAMRA-labeled Ac-TZ14011 were 11 and 14 nM, respectively. These values indicated that fluorophore labeling does not inhibit binding of Ac-TZ14011 as reported elsewhere about binding of TAMRA-Ac-TZ14011 (*19*).

The binding of TAMRA-Ac-TZ14011 to a cell membrane was observed with a laser-scanning confocal microscope to determine the specific binding of Ac-TZ14011 to CXCR4. The CXCR4-GFP fusion protein was stably expressed in the NP-2 cell line (*20*), and TAMRA-Ac-TZ14011 binding to CXCR4 was clearly observed at the membrane in the absence of competitors (Figure 2A). To assess the specific binding of ligands, excess unlabeled Ac-TZ14011 was added to the medium with TAMRA-Ac-TZ14011. Upon addition of Ac-TZ14011, weak fluorescence intensity was observed on the cell membrane or cytoplasm (Figure 2B). Vesicles observed in the cytoplasm show internalization of CXCR4 receptors induced by binding of the ligands, and signals from GFP and TAMRA showed colocalization in the cytoplasm. These results indicate the specific binding of TAMRA-Ac-TZ14011 to CXCR4. To evaluate the binding specificity for CXCR4 across the different kinds of GPCRs, HeLa cells, which stably express CD4-CCR5, were utilized for microscopy assays. The binding of TAMRA-Ac-TZ14011 was observed as for the NP-2 CXCR4-GFP cell line (Figure 2C). With the addition of excess CXCL12 (Figure

* To whom correspondence should be addressed. E-mail: tamamura.mr@tmd.ac.jp.
[†] Tokyo Medical and Dental University.
[‡] National Institute of Infectious Diseases.

[1]Abbreviations: Ac, acetyl; Cit, L-citrulline; DIC, differential interference contrast; ESI-MS, electron spray ionization-mass spectrometry; FBS, fetal bovine serum; Fmoc, 9-fluorenylmethoxycarbonyl; GPCR, G-protein-coupled receptor; HEPES, 4-(2-hydroxyethyl)-1-piperazineethanesulfonic acid; Nal, L-3-(2-naphthyl)alanine; Nal(1), L-3-(1-naphthyl)alanine; RI, radioisotope; RP-HPLC, reverse-phase HPLC; TAMRA, tetramethylrhodamine; TFA, trifluoroacetic acid.

10.1021/bc800216p CCC: $40.75
Published on Web 08/16/2008

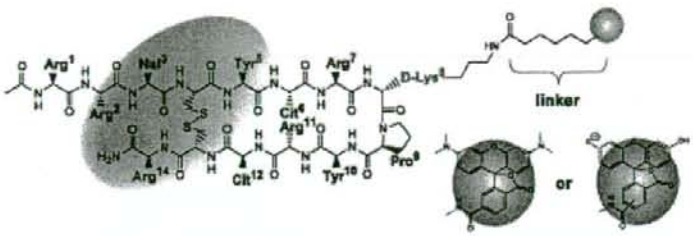

Figure 1. Design of fluorophore-labeled Ac-TZ14011. The amino acid residues in the red area are critical to CXCR4 binding activity. Fluorophores are shown as blue spheres.

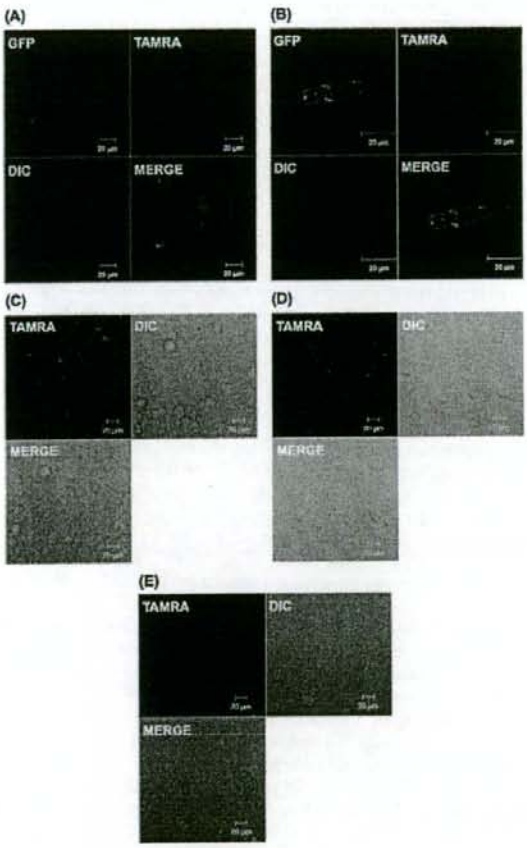

Figure 2. Confocal microscopy assays of TAMRA-Ac-TZ14011 binding to CXCR4. The signals of GFP and TAMRA are displayed in green and red, respectively. (A) Binding to NP2-GFP-CXCR4 cells. (B) Competitive binding to NP2 cells with excess amount of Ac-TZ14011. (C) Binding to HeLa-CD4-CCR5 cells. (D) Competitive binding to HeLa-CD4-CCR5 cells with excess CXCL12. (E) Competitive binding to HeLa-CD4-CCR5 cells with excess Ac-TZ14011. Descriptions of images are indicated in the pictures.

2D) or Ac-TZ14011 (Figure 2E), the fluorescence intensity on the cell membrane was decreased. These results show that TAMRA-Ac-TZ14011 binds specifically to CXCR4 but not to CCR5.

To investigate the utility of fluorescein-labeled Ac-TZ14011, cell-based binding assays were performed. In this binding assay, fluorescein-Ac-TZ14011 was utilized as a competitor to derivatives of FC131 (*8*) and the dipicolylamine-*p*-xylene Zn(II)

Table 1. K_d Values Determined by RI-Competition and Fluorescent Probe Competition Assays

	IC_{50} (nM)		
	[^{125}I]-CXCL12 competition ($IC_{50}C$)	fluorescein-Ac-TZ14011 competition ($IC_{50}F$)	$IC_{50}F/IC_{50}C$
T140	3.93	24.7	6.3
Zn^{2+}-(Dpa)-*p*-Xyl	47[a]	291	6.2
FC131	14.6	109	7.5

[a] This value is derived from ref *18*.

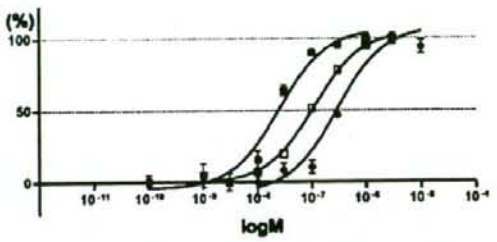

Figure 3. Curve fitting for CXCR4 binding of T140 (■), Zn^{2+}-(Dpa)-*p*-Xyl (●), and FC131 (□) in competitive assays by fluorescein-Ac-TZ14011. The *x* and *y* axes show concentrations and inhibition percentages of the binding of test compounds, respectively.

complex [Zn^{2+}-(Dpa)-*p*-Xyl] that were developed as CXCR4 antagonists (Figure 3) (*21*). The binding constants of these compounds were previously estimated by competitive assays with [^{125}I]-CXCL12. As a result, larger values of IC_{50} than those in the previous assays were observed (Table 1). The difference of the binding constants of competitors was assumed to be a reflection of the difference of IC_{50} values in the assays. It is especially interesting that the values of IC_{50} as determined by fluorescent- and RI-competition assays are clearly correlated. It was clearly indicated that binding activity of compounds can be estimated by binding inhibition assays conducted at a constant concentration of compounds. Indeed, in the detailed binding assays, a significant correlation was observed in IC_{50} values measured by both methods for T140, TC13, and TC22.

In the application of high-throughput screening for pharmacophores of CXCR4 ligands, it is important to be able to rapidly determine IC_{50} values. To test whether fluorescein-Ac-TZ14011 could be useful as a ligand in high-throughput screening, binding inhibition analyses at constant compound concentrations were performed. Twenty-four derivatives of a cyclic pentapeptide, FC131, were prepared for the analyses as described previously (Figure 4A) (*8*). The conditions used were the same as in the binding experiments shown in Figure 3 except that the compound concentration was kept constant at 2 μM. Nine compounds were found to induce >75% inhibition at this concentration (Figure 4B). The IC_{50} values of compounds that showed high inhibitory scores in the screening analyses were examined

(A)

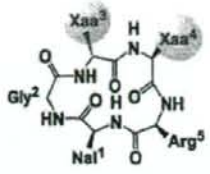

compound	Xaa^3	Xaa^4	compound	Xaa^3	Xaa^4
1	Arg	Nal	13	Arg	D-Nal
2	Nal	Arg	14	Nal	D-Arg
3	Arg	Trp	15	Arg	D-Trp
4	Trp	Arg	16	Trp	D-Arg
5	Arg	Nal(1)	17	Arg	D-Nal(1)
6	Nal(1)	Arg	18	Nal(1)	D-Arg
7	D-Arg	Nal(1)	19	D-Arg	D-Nal
8	D-Nal	Arg	20	D-Nal	D-Arg
9	D-Arg	Trp	21	D-Arg	D-Trp
10	D-Trp	Arg	22	D-Trp	D-Arg
11	D-Arg	Nal(1)	23	D-Arg	D-Nal(1)
12	D-Nal(1)	Arg	24	D-Nal(1)	D-Arg

(B)

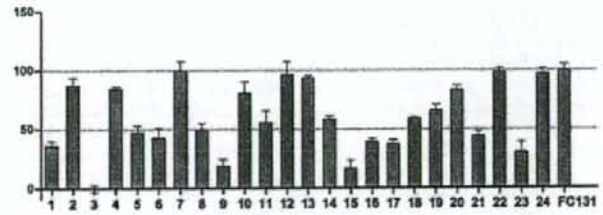

(C)

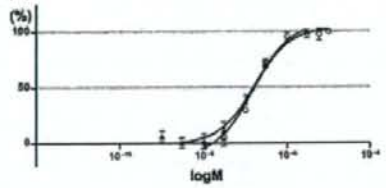

(D)

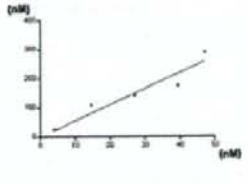

Figure 4. (A) Design of cyclic pentapeptides. Xaa^3 and Xaa^4 (red area) were manually randomized. (B) Results of single concentration point assays for determination of the binding activity of library compounds at one time. The *x* and *y* axes show concentrations and inhibition percentages of binding of test compounds, respectively. Data were measured in triplicate, and error bars show the SEM. (C) Curve fitting for CXCR4 binding of TC13 (○) and TC22 (▲) in competitive assays by fluorescein-Ac-TZ14011. The *x* and *y* axes show concentrations and inhibition percentages of binding of test compounds, respectively. (D) Correlation between IC_{50} values determined by RI-competition assays (*x*-axis) and fluorescein-Ac-TZ14011 competition assays (*y*-axis). The compound and IC_{50} values are shown in Tables 1 and 2. The *P* value determined from correlation analysis was 0.012.

Table 2. K_d Values Determined by RI-Competition and Fluorescent Probe Competition Assays

	IC_{50} (nM)		
	[^{125}I]-CXCL12 competition ($IC_{50}C$)	fluorescein-Ac-TZ14011 competition ($IC_{50}F$)	$IC_{50}F/IC_{50}C$
T140	3.93	24.7	6.3
TC13	27.0	143	5.3
TC22	39.4	176	4.5

further (Table 2). The IC_{50} values of TC13 and TC22 were determined to be 143 and 176 nM, respectively (Figure 4C). The IC_{50} values determined in this assay showed a clear correlation with those in RI-competition assays (Figure 4D, manuscript in preparation).

Advantages of the fluorescence-based analyses include their utility in high-throughput screening and direct observation of the binding state on cell membrane by fluorescence microscope; binding assays and confocal microscopy study were performed to evaluate these advantages. The binding of T140 was previously assessed with site-directed mutagenesis of CXCR4, which indicated that the extracellular loop 2 of the receptor is the main target for this peptide (*22*). The observation of Ac-TZ14011 binding to cell membranes provided convincing evidence of specificity for the target receptor. Competition with excess unlabeled Ac-TZ14011 and CXCL12 showed clear inhibition of TAMRA-Ac-TZ14011 binding. There has been concern that CXCR4 ligands could bind nonspecifically to other GPCRs. A binding study utilizing CCR5-CD4-HeLa cells showed evidence of a high degree of specificity of the ligands. HeLa cells naturally express CXCR4 (*23*), and in the event of overexpression of CCR5-CD4 on the membrane, the binding of TAMRA-Ac-TZ14011 was prevented by the addition of competitors. These results indicate that these peptides bind to the same target site on the cell membrane, CXCR4. Internalization of CXCR4 stimulated by binding of ligands was clearly observed, particularly in the presence of competitors indicating that ligands bound to CXCR4 are simultaneously incorporated in the cytoplasm. Interestingly, on the basis of the numbers and size of vesicles observed, CXCL12 showed stronger induction of CXCR4 internalization than Ac-TZ14011. Promotion of CXCR4 internalization is one of the important mechanisms for inhibition of HIV entry (*24*). The difference of ligand-dependent effects on CXCR4 internalization will be studied further in our laboratory.

In conclusion, the structure−activity relationships of ligands for CXCR4 have been well studied, but relatively few known ligand pharmacophores have been studied because of the difficulty associated with the analysis of receptor−ligand interactions. Our results strongly indicate that fluorescence-based ligand binding assays could be useful in the exploration of novel pharmacophores for CXCR4 ligands and that such compounds have promise as therapeutic agents for AIDS, breast cancer metastasis, and rheumatoid arthritis. Furthermore, this methodology is applicable to the design of ligands for other GPCRs.

ACKNOWLEDGMENT

We are grateful to Professor Kazunari Akiyoshi for his generous cooperation in experiments. This research was supported in part by a Grant-in-Aid for Scientific Research from the Ministry of Education, Culture, Sports, Science and Technology, Japan, and Health and Labour Sciences Research Grants.

Supporting Information Available: Detailed materials and methods. This material is available free of charge via the Internet at http://pubs.acs.org.

LITERATURE CITED

(1) Oberlin, E., Amara, A., Bachelerie, F., Bessia, C., Virelizier, J. L., Arenzana-Seisdedos, F., Schwartz, O., Heard, J. M., Clark-Lewis, I., Legler, D. F., Loetscher, M., Baggiolini, M., and Moser, B. (1996) The CXC chemokine SDF-1 is the ligand for LESTR/fusin and prevents infection by T-cell-line-adapted HIV-1. *Nature 382*, 833–835.

(2) Bleul, C. C., Farzan, M., Choe, H., Parolin, C., Clark-Lewis, I., Sodroski, J., and Springer, T. A. (1996) The lymphocyte chemoattractant SDF-1 is a ligand for LESTR/fusin and blocks HIV-1 entry. *Nature 382*, 829–833.

(3) Baird, A. M., Gerstein, R. M., and Berg, L. J. (1999) The role of cytokine receptor signaling in lymphocyte development. *Curr. Opin. Immunol. 11*, 157–166.

(4) Koshiba, T., Hosotani, R., Miyamoto, Y., Ida, J., Tsuji, S., Nakajima, S., Kawaguchi, M., Kobayashi, H., Doi, R., Hori, T., Fujii, N., and Imamura, M. (2000) Expression of stromal cell-derived factor 1 and CXCR4 ligand receptor system in pancreatic cancer: a possible role for tumor progression. *Clin. Cancer Res. 6*, 3530–3535.

(5) Nanki, T., Hayashida, K., El-Gabalawy, H. S., Suson, S., Shi, K., Girschick, H. J., Yavuz, S., and Lipsky, P. E. (2000) Stromal cell-derived factor-1-CXC chemokine receptor 4 interactions play a central role in $CD4^+$ T cell accumulation in rheumatoid arthritis synovium. *J. Immunol. 165*, 6590–6598.

(6) Feng, Y., Broder, C. C., Kennedy, P. E., and Berger, E. A. (1996) HIV-1 entry cofactor: functional cDNA cloning of a seven-transmembrane, G protein-coupled receptor. *Science 272*, 872–7.

(7) Tamamura, H., Xu, Y., Hattori, T., Zhang, X., Arakaki, R., Kanbara, K., Omagari, A., Otaka, A., Ibuka, T., Yamamoto, N., Nakashima, H., and Fujii, N. (1998) A low-molecular-weight inhibitor against the chemokine receptor CXCR4: a strong anti-HIV peptide T140. *Biochem. Biophys. Res. Commun. 25*, 877–882.

(8) Fujii, N., Oishi, S., Hiramatsu, K., Araki, T., Ueda, S., Tamamura, H., Otaka, A., Kusano, S., Terakubo, S., Nakanishi, H., Broach, J. A., Trent, J. O., Wang, Z., and Peiper, S. C. (2003) Molecular-size reduction of a potent CXCR4-chemokine antagonist using orthogonal combination of conformation- and sequence-based libraries. *Angew. Chem., Int. Ed. 42*, 3251–3.

(9) Ichiyama, K., Yokoyama-Kumakura, S., Tanaka, Y., Tanaka, R., Hirose, K., Bannai, K., Edamatsu, T., Yanaka, M., Niitani, Y., Miyano-Kurosaki, N., Takaku, H., Koyanagi, Y., and Yamamoto, N. (2003) A duodenally absorbable CXC chemokine receptor 4 antagonist, KRH-1636, exhibits a potent and selective anti-HIV-1 activity. *Proc. Natl. Acad. Sci. U.S.A. 100*, 4185–4190.

(10) Donzella, G. A., Schols, D., Lin, S. W., Esté, J. A., Nagashima, K. A., Allaway, G. P., Sakmar, T. P., Henson, G., De Clercq, E., and Moore, J. P. (1998) AMD3100, a small molecule inhibitor of HIV-1 entry via the CXCR4 co-receptor. *Nat. Med. 4*, 72–77.

(11) Grynkiewicz, G., Poenie, M., and Tsien, R. Y. (1985) A new generation of Ca^{2+} indicators with greatly improved fluorescence properties. *J. Biol. Chem. 260*, 3440–3450.

(12) Kiyose, K., Kojima, H., Urano, Y., and Nagano, T. (2006) Development of a ratiometric fluorescent zinc ion probe in near-infrared region, based on tricarbocyanine chromophore. *J. Am. Chem. Soc. 128*, 6548–6549.

(13) Takakusa, H., Kikuchi, K., Urano, Y., Sakamoto, S., Yamaguchi, K., and Nagano, T. (2002) Design and synthesis of an enzyme-cleavable sensor molecule for phosphodiesterase activity based on fluorescence resonance energy transfer. *J. Am. Chem. Soc. 124*, 1653–1657.

(14) Kojima, H., Urano, Y., Kikuchi, K., Higuchi, T., Hirata, Y., and Nagano, T. (1999) Fluorescent indicators for imaging nitric oxide production. *Angew. Chem., Int. Ed. 38*, 3209–3212.

(15) Ojida, A., Mito-oka, Y., Sada, K., and Hamachi, I. (2004) Molecular recognition and fluorescence sensing of monophosphorylated peptides in aqueous solution by bis(zinc(II)-dipicolylamine)-based artificial receptors. *J. Am. Chem. Soc. 126*, 2454–2463.

(16) Tamamura, H., Omagari, A., Oishi, S., Kanamoto, T., Yamamoto, N., Peiper, S. C., Nakashima, H., Otaka, A., and Fujii, N. (2000) Pharmacophore identification of a specific CXCR4 inhibitor, T140, leads to development of effective anti-HIV agents with very high selectivity indexes. *Bioorg. Med. Chem. Lett. 10*, 2633–2637.

(17) Tamamura, H., Hiramatsu, K., Mizumoto, M., Ueda, S., Kusano, S., Terakubo, S., Akamatsu, M., Yamamoto, N., Trent, J. O., Wang, Z., Peiper, S. C., Nakashima, H., Otaka, A., and Fujii, N. (2003) Enhancement of the T140-based pharmacophores leads to the development of more potent and bio-stable CXCR4 antagonists. *Org. Biomol. Chem. 1*, 3663–3669.

(18) Hanaoka, H., Mukai, T., Tamamura, H., Mori, T., Ishinoa, S., Ogawa, K., Iida, Y., Doi, R., Fujii, N., and Saji, H. (2006) Development of a 111In-labeled peptide derivative targeting a chemokine receptor, CXCR4, for imaging tumors. *Nucl. Med. Biol. 33*, 489–494.

(19) Oishi, S., Masuda, R., Evans, B., Ueda, S., Goto, Y., Ohno, H., Hirasawa, A., Tsujimoto, G., Wang, Z., Peiper, S. C., Naito, T., Kodama, E., Matsuoka, M., and Fujii, N. (2008) Synthesis and application of fluorescein- and biotin-labeled molecular probes for the chemokine receptor CXCR4. *ChemBioChem 9*, 1154–1158.

(20) Futahashi, Y., Komano, J., Urano, E., Aoki, T., Hamatake, M., Yoshida, T., Koyanagi, Y., Matsuda, Z., and Yamamoto, N. (2007) Separate elements are required for ligand-dependent and -independent internalization of metastatic potentiator CXCR4. *Cancer Sci. 98*, 373–379.

(21) Tamamura, H., Ojida, A., Ogawa, T., Tsutsumi, H., Masuno, H., Nakashima, H., Yamamoto, N., Hamachi, I., and Fujii, N. (2006) Identification of a new class of low molecular weight antagonists against the chemokine receptor CXCR4 having the dipicolylamine-zinc(II) complex structure. *J. Med. Chem. 49*, 3412–3415.

(22) Trent, J. O., Wang, Z., Murray, J. L., Shao, W., Tamamura, H., Fujii, N., and Peiper, S. C. (2003) Lipid bilayer simulations of CXCR4 with inverse agonists and weak partial agonists. *J. Biol. Chem. 278*, 47136–47144.

(23) Valente, S. T., Chanel, C., Dumonceaux, J., Olivier, R., Marullo, S., Briand, P., and Hazan, U. (2001) CXCR4 is down-regulated in cells infected with the CD4-independent X4 human immunodeficiency virus type 1 isolate m7NDK. *J. Virol. 75*, 439–447.

(24) Orsini, M. J., Parent, J. L., Mundell, S. J., Marchese, A., and Benovic, J. L. (1999) Trafficking of the HIV coreceptor CXCR4. Role of arrestins and identification of residues in the C-terminal tail that mediate receptor internalization. *J. Biol. Chem. 274*, 31076–31086.

BC800216P

A New Humanized Mouse Model of Epstein-Barr Virus Infection That Reproduces Persistent Infection, Lymphoproliferative Disorder, and Cell-Mediated and Humoral Immune Responses

Misako Yajima,[1,a] Ken-Ichi Imadome,[1,a] Atsuko Nakagawa,[2] Satoru Watanabe,[3] Kazuo Terashima,[4] Hiroyuki Nakamura,[1] Mamoru Ito,[6] Norio Shimizu,[3] Mitsuo Honda,[5] Naoki Yamamoto,[4,5] and Shigeyoshi Fujiwara[1]

[1]Department of Infectious Diseases, National Research Institute for Child Health and Development, [2]Pathology Laboratory, Department of Clinical Laboratory Medicine, National Center for Child Health and Development, [3]Department of Virology, Division of Medical Science, Medical Research Institute, and [4]Department of Molecular Virology, Graduate School of Medicine, Tokyo Medical and Dental University, and [5]AIDS Research Center, National Institute of Infectious Diseases, Tokyo, and [6]Central Institute for Experimental Animals, Kawasaki, Japan

The functional human immune system, including T, B, and natural killer lymphocytes, is reconstituted in NOD/Shi-*scid*/IL-2Rγ^{null} (NOG) mice that receive hematopoietic stem cell transplants. Here, we show that these humanized mice can recapitulate key aspects of Epstein-Barr virus (EBV) infection in humans. Inoculation with $\sim 1 \times 10^3$ TD_{50} (50% transforming dose) of EBV caused B cell lymphoproliferative disorder, with histopathological findings and latent EBV gene expression remarkably similar to that in immunocompromised patients. Inoculation with a low dose of virus ($\leq 1 \times 10^1$ TD_{50}), in contrast, resulted in apparently asymptomatic persistent infection. Levels of activated $CD8^+$ T cells increased dramatically in the peripheral blood of infected mice, and enzyme-linked immunospot assay and flow cytometry demonstrated an EBV-specific T cell response. Immunoglobulin M antibody specific to the EBV-encoded protein BFRF3 was detected in serum from infected mice. The NOG mouse is the most comprehensive small-animal model of EBV infection described to date and should facilitate studies of the pathogenesis, prevention, and treatment of EBV infection.

Epstein-Barr virus (EBV) is a tumor virus associated with a variety of malignancies, including Burkitt lymphoma, nasopharyngeal carcinoma, and Hodgkin lymphoma [1]. It is also an etiological agent of infectious mononucleosis (IM), which is characterized by transient proliferation of EBV-infected B lymphoblastoid cells and an excessive anti-EBV T cell response. EBV has a unique ability to growth transform human B lymphocytes in vitro and establish lymphoblastoid cell lines (LCLs) [2]. EBV-transformed lymphoblasts express 6 nuclear proteins (Epstein-Barr nuclear antigen [EBNA] 1, 2, 3A, 3B, 3C, and LP) and 3 membrane proteins (latent membrane protein [LMP] 1, 2A, and 2B), and this pattern of EBV gene expression is termed latency III. In contrast, Burkitt lymphoma cells express only EBNA1 consistently (latency I), whereas Hodgkin lymphoma and nasopharyngeal carcinoma cells express EBNA1, LMP1, and LMP2 (latency II). In vivo, EBV-transformed cells are effectively removed by virus-specific cytotoxic T cells, and EBV infection in immunocompetent humans is usually subclinical, except for IM caused by primary infection during adolescence or adulthood. However, in immunocompromised hosts, such as patients with AIDS and transplant recipients, EBV-infected B lymphoblasts can proliferate and cause lymphoproliferative disorder.

Received 28 December 2007; accepted 19 March 2008; electronically published 15 July 2008.

Potential conflicts of interest: none reported.

Financial support: Ministry of Health, Labour, and Welfare of Japan (grants H18-Shinko-013 and H19-AIDS-003).

* M.Y. and K.-I.I. contributed equally to this study.

Reprints or correspondence: Dr. Shigeyoshi Fujiwara, Dept. of Infectious Diseases, National Research Institute for Child Health and Development, 2-10-1 Okura, Setagaya-ku, Tokyo 157-8535, Japan (shige@nch.go.jp); or, Dr. Norio Shimizu, Dept. of Virology, Div. of Medical Science, Medical Research Institute, Tokyo Medical and Dental University, 1-5-45 Yushima, Bunkyo-ku, Tokyo 113-8519, Japan (nshivir@tmd.ac.jp); or, Dr. Naoki Yamamoto, AIDS Research Center, National Institute of Infectious Diseases, 1-23-1 Toyama, Shinjuku-ku, Tokyo 162-8640, Japan (nyama@nih.go.jp).

The Journal of Infectious Diseases 2008; 198:673–82

0022-1899/2008/19805-0008$15.00
DOI: 10.1086/590502

EBV infects only humans in nature and limited animal species under experimental conditions. It can infect cotton-top tamarins and induce lymphomas, which have been used as a model of EBV-associated lymphomas [3, 4]. Nonhuman primates possess their own lymphocryptoviruses related to EBV, and research on the use of these virus-host systems as models of EBV infection is currently in progress [5, 6]. Small-animal models of EBV have also been developed, which are particularly useful when a large number of animals are necessary. *Scid* mice that receive intraperitoneal transplants of EBV-transformed LCLs or peripheral blood mononuclear cells (PBMCs) isolated from EBV-infected persons develop lymphomas, which have been used as a model of human lymphoproliferative disorder [7–9]. Recently, NOD/*scid* mice transplanted with human hematopoietic stem cells (HSCs) and reconstituted mainly with B lymphocytes were infected with EBV, and the development of lymphoproliferative disorder was described [10]. The immune response to EBV was not studied in these *scid* or NOD/*scid* mouse models. Very recently, a functional human immune system could be reconstituted in highly immunodeficient mouse strains, and these so-called humanized mice were shown able to mount an EBV-specific T cell response [11, 12]. These studies were, however, performed mainly using immunological standpoints and did not provide detailed virological data.

NOD/Shi-*scid*/IL-2Rγ^{null} (referred to here as NOG) is a highly immunodeficient mouse strain that was developed very recently and that, after transplantation with cord blood HSCs, is able to reconstitute most major components of the hematolymphoid system, including T cells, B cells, NK cells, macrophages, and dendritic cells [13–15]. Human T cells that develop in NOG mice are functional in that they can be activated to display cytotoxic activity [15, 16]. These properties made NOG mice an excellent model of human virus infections targeting the immune system, such as those with human T-lymphotropic virus–1 and HIV-1 [17–20]. Here, we provide evidence that humanized NOG mice can reproduce various key aspects of human EBV infection and propose that they may be a valuable tool for studies of EBV infection.

Table 1. Primers for reverse-transcription polymerase chain reaction to detect Epstein-Barr virus (EBV) transcripts.

Transcript, primer	Sequence (5'→3')
EBNA1	
5'	gatgagcgtttgggagagctgattctgca
3'	tcctcgtccatggttatcac
EBNA2	
5'	agaggaggtggtaagcggttc
3'	tgacgggtttccaagactatcc
LMP1	
5'	ctctccttctcctcctcttg
3'	caggagggtgatcatcagta
LMP2A	
5'	atgactcatctcaacacata
3'	catgttaggcaaattgcaaa
LMP2B	
5'	cagtgtaatctgcacaaaga
3'	catgttaggcaaattgcaaa
EBER1	
5'	agcacctacgctgccctaga
3'	aaaacatgcggaccaccagc
BZLF1 (first)	
5'	attgcaccttgccgccaccttg
3'	cgcatttttctggaagccacccga
BZLF1 (second)	
5'	gaccaagctaccagagtctat
3'	cagaatcgcattcctccagcga
BMRF1	
5'	ctagccgtcctgtccaagtgc
3'	agccaaacagctccttgccca
BLLF1	
5'	gtcagtacaccatccagagcc
3'	ttggtagacagccttcgtatg
GAPDH	
5'	gcctcctgcaccaccaactg
3'	cgacgcctgcttcaccaccctct

NOTE. EBNA, Epstein-Barr nuclear antigen; EBER, EBV-encoded small RNA; LMP, latent membrane protein.

METHODS

Preparation of humanized mice. NOG mice were obtained from the Central Institute for Experimental Animals (Kawasaki, Japan). Protocols for experiments with NOG mice were approved by the Institutional Animal Care and Use Committee of the National Institute of Infectious Diseases (NIID). Cord blood was supplied by the Tokyo Cord Blood Bank after obtaining informed consent. The use of human materials in this research was approved by the institutional review boards of the National Research Institute for Child Health and Development, the NIID, the Tokyo Medical and Dental University, and the Tokyo Cord Blood Bank. The isolation of human CD34$^+$ HSCs from cord blood by means of the MACS Direct CD34 Progenitor Cell Isolation Kit (Miltenyi Biotec), their intravenous injection (1×10^4 to 1.2×10^5 cells/mouse) into 6–10-week-old female NOG mice, and the characterization of the reconstitution of the human hematoimmune system were done as described elsewhere [18, 20]. NOG mice in which the human hematoimmune system was reconstituted are referred here as humanized NOG (hNOG) mice.

Experimental EBV infection, quantification of viral DNA, and detection of viral mRNAs. Virus production by EBV-infected Akata cells was stimulated by brief treatment with anti-IgG antibody (Dako), and culture fluid was used as inoculum after filtration through a 0.45-μm membrane filter [21]. For virus titration, cord blood lymphocytes were plated at the density

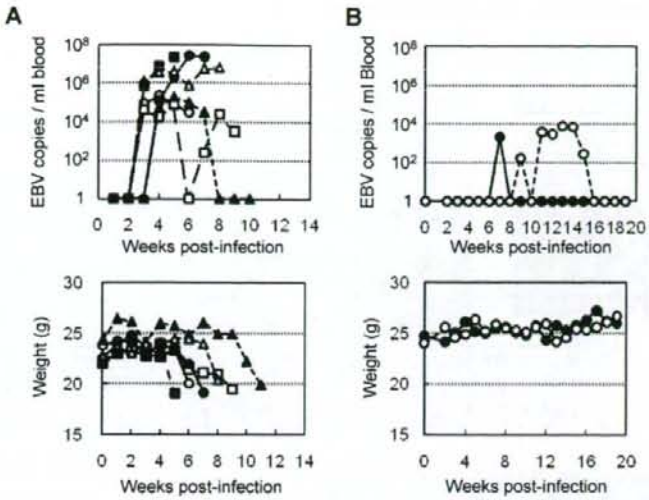

Figure 1. Peripheral blood Epstein-Barr virus (EBV) DNA load and body weight in humanized NOG (hNOG) mice infected with EBV. *A*, Infection at a high dose of virus. Six mice were inoculated intravenously with 1×10^3 TD_{50} of EBV. Peripheral blood EBV DNA load *(upper panels)* and body weight *(lower panels)* were then determined weekly. Each symbol in the graphs represents an individual mouse. Interruption of records indicates the death or killing of a mouse. *B*, Infection at lower doses. Peripheral blood EBV DNA load *(upper panel)* and body weight *(lower panel)* of 2 mice inoculated with low doses of EBV (*black circle*, 1×10^{-1} TD_{50}; *white circle*, 1×10^1 TD_{50}) are shown.

of 2×10^5 cells per well in 6-well plates and then inoculated with serial 10-fold dilutions of virus preparation. The number of wells with proliferating lymphocytes was counted 6 weeks after infection, and the titer of the virus in 50% transforming dose (TD_{50}) was determined by the Reed-Muench method [22]. EBV was inoculated intravenously through the tail vein. EBV DNA was quantified by a real-time quantitative polymerase chain reaction (PCR) assay based on the TaqMan system (Applied Biosystems), as described elsewhere [23]. Analysis of EBV gene expression by reverse-transcription PCR (RT-PCR) was done as described elsewhere, using the primers listed in table 1 [24].

Histopathology, in situ hybridization (ISH), and immunohistochemistry. Tissue samples were fixed in 10% buffered formalin, embedded in paraffin, and stained with hematoxylin-eosin. For phenotypic analysis of proliferating lymphocytes, immunostaining for CD3 (Nichirei), CD4 (Novocastra), CD8 (Nichirei), CD45RO, CD20, CD79a, CD30, Mum1 (Dako), CD23, CD10, CD56 (Novocastra), granzyme B (Dako), and T cell intracellular antigen 1 (Beckman Coulter) was performed on paraffin sections. EBV was detected by immunostaining for LMP1 and EBNA2 (Dako) and by ISH with EBV-encoded small RNA (EBER) probe. Immunohistochemistry and ISH were performed on an automated stainer (Benchmark XT; Ventana Medical Systems), in accordance with the manufacturer's recommendations. To determine the cell lineage of EBV-infected cells, paraffin sections were applied to double staining with EBER ISH and immunohistochemistry.

Detection of EBV-specific T cell response. Enzyme-linked immunospot (ELISPOT) assay was performed with the Immunocyto IFN-γ ELISPOT Kit (MBL), in accordance with the instructions supplied by the manufacturer. Briefly, $CD8^+$ T cells were isolated from PBMCs from EBV-infected hNOG mice with the IMag anti-human CD8 Particles–DM (BD Biosciences). Mixture of these $CD8^+$ T cells and an autologous LCL were incubated with interleukin (IL)–2 in microplates coated with antibody to interferon (IFN)–γ for 17 h. Captured IFN-γ was detected by use of biotinated antibody to IFN-γ and alkaline phosphatase–conjugated streptavidin and was visualized by reaction with the BCIP/NBT chromogen substrate. The unpaired Student's *t* test was used for statistical analysis. IFN-γ secretion in response to EBV was also examined by flow cytometry, as described elsewhere [25]. Briefly, aliquots of murine splenocytes and an LCL were mixed in 6-well plates in the presence of brefeldin A (10 μg/mL) and incubated at 37°C in 5% CO_2 for 17 h. After incubation, the cell suspensions were stained with phycoerythrin-conjugated anti-human CD69, phycoerythrin–Texas red–conjugated anti-human CD45, and phycoerythrin–cyanin 5–conjugated anti-human CD8 for 30 min at 4°C and were fixed with 2% paraformaldehyde. Cells were then permeabilized and stained with BD Perm/Wash buffer (BD Biosciences) containing fluorescein isothiocyanate–conjugated anti-human IFN-γ for 30 min at 4°C. Stained cells were analyzed using an EpicsXL flow cytometer (Beckman Coulter).

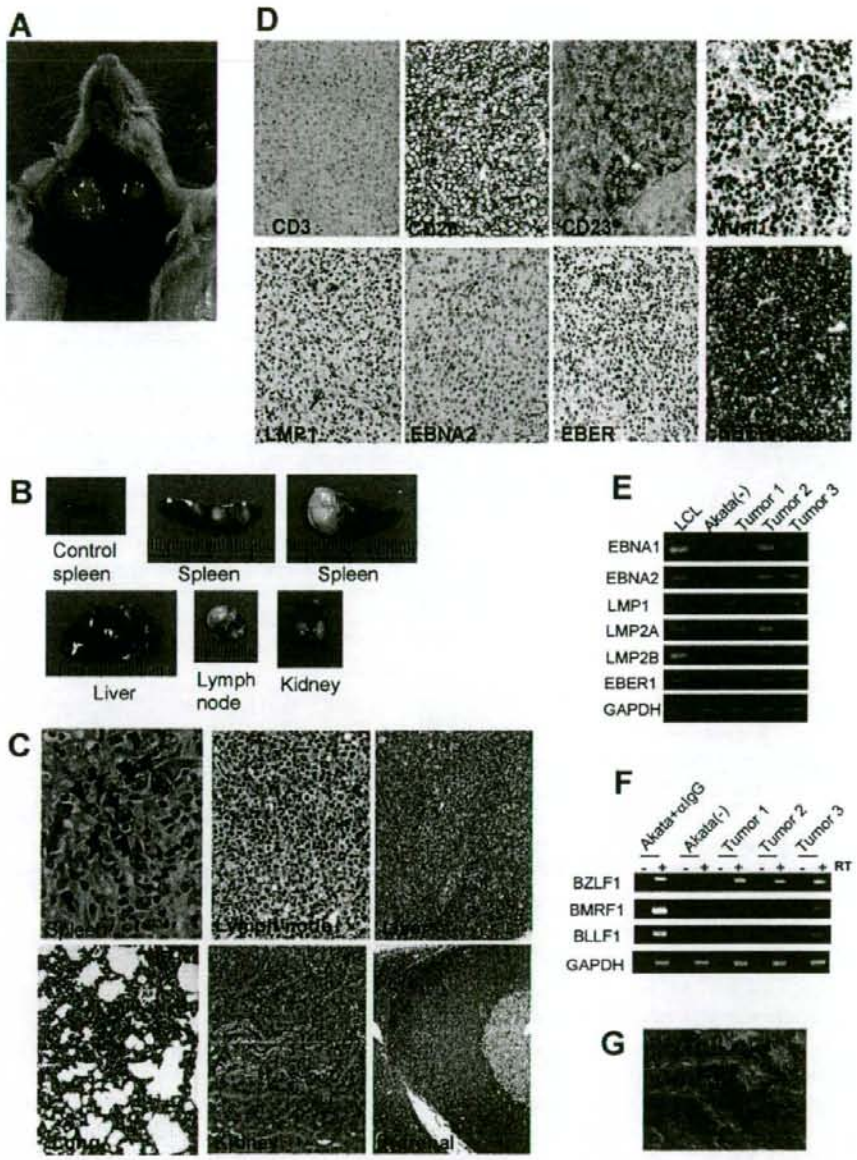

Figure 2. Pathological and virological analyses of Epstein-Barr virus (EBV)–infected humanized NOG (hNOG) mice. *A*, Photograph of an EBV-infected mouse showing tumors in the cervical area. *B*, Photographs of spleens, liver, lymph node, and kidney from EBV-infected mice with lymphoproliferative disorder. The upper left panel shows the spleen from an uninfected mouse. *C*, Photomicrographs of hematoxylin-eosin–stained tissues from mice with lymphoproliferative disorder. The arrow indicates a Reed-Stemberg–like cell, and the arrowheads indicate Hodgkin-like cells. Original magnifications, ×1000 for spleen, ×400 for lymph node, and ×200 for liver, lung, kidney, and adrenal gland. *D*, Immunohistochemical staining for lymphocyte surface markers (CD3, CD20, CD23, and Mum1) and EBV-encoded proteins (latent membrane protein [LMP] 1 and Epstein-Barr nuclear antigen [EBNA] 2), as well as in situ hybridization for EBV-encoded small RNA (EBER), in a lymph node from a mouse with lymphoproliferative disorder. The bottom right panel represents double staining for EBER and CD20. Original magnifications, ×200 for all except EBER/CD20, which is ×400. *E* and *F*, Reverse-transcription polymerase chain reaction detection of latent-cycle *(E)* and lytic-cycle *(F)* EBV gene expression in tumors from EBV-infected hNOG mice. Spleen tumors from 3 different mice were examined for the expression of EBNA1, EBNA2, LMP1, LMP2A, LMP2B, EBER1, BZLF1, BMRF1, and BLLF1. RNA samples from a lymphoblastoid cell line (LCL) *(E)* and anti-IgG–treated Akata cells *(F)* were used as positive controls, and an RNA sample from EBV-negative Akata cells (*E* and *F*) was used as a negative control. Assays were done with (+) or without (−) reverse transcriptase (RT) in panel F. Expression of GAPDH was examined as a reference. *G*, Double staining of EBER and CD20 in the liver of an hNOG mouse that was persistently infected with EBV without developing lymphoproliferative disorder. EBER is stained navy in the nucleus, and CD20 is stained brown in the membrane. Original magnification, ×1000.

Table 2. Quantification of Epstein-Barr virus (EBV) DNA in persistently infected humanized NOG mice.

Organ	Mouse	
	N35-1[a]	N35-3[b]
Bone marrow	ND	4.1×10^4
Spleen	6.2×10^2	5.7×10^3
Liver	ND	2.7×10^4
Lymph node (neck)	1.6×10^3	6.9×10^3
Lymph node (axilla)	ND	2.6×10^2
Lymph node (mesentery)	ND	4.1×10^2
Lungs	2.7×10^3	1.0×10^4
Kidneys	1.2×10^3	4.8×10^4
Adrenal gland	4.4×10^1	8.0×10^5

NOTE. Data are the amounts of EBV DNA measured 22 weeks after infection, in copies per microgram of DNA. ND, not detectable.

[a] Infected at 1×10^{-1} TD_{50}.

[b] Infected at 1×10^1 TD_{50}.

Detection of antibodies specific to EBV. IgM antibody to the EBV BFRF3 protein was detected by immunoblotting essentially as described elsewhere [24], except that horseradish peroxidase–conjugated antibody specific to human IgM (Beckman Coulter) was used as secondary antibody. To prepare the glutathione *s*-transferase (GST)–BFRF3 fusion protein, a DNA fragment spanning the entire coding region of BFRF3 was amplified by PCR (sense primer, 5'-GGCTCGAATTCATGGCACGCCG-GCTGCCC-3'; antisense primer, 5'-GGCTCGGATCCATAC-ACCATGTTTCGTGCCC-3') and inserted to the GST fusion vector pSGENT2, to yield the plasmid pSGENT2-BFRF3. *Escherichia coli* cells harboring pSGENT2-BFRF3 were stimulated with isopropyl β-D-1-thiogalactopyranoside to induce the expression of GST-BFRF3, which was subsequently purified by use of the Bulk GST Purification Module (GE Healthcare).

RESULTS

EBV infection in hNOG mice. Transplantation of human $CD34^+$ HSCs in NOG mice and reconstitution of the human hematoimmune system were done as described elsewhere [18, 20]. In the initial attempts at infection, 1×10^3 TD_{50} of the Akata strain of EBV was inoculated into 6 hNOG mice, and EBV DNA was demonstrated in the peripheral blood of all of them (figure 1*A*). EBV DNA was first evident at 3–4 weeks after inoculation and reached peak levels of $\sim 1 \times 10^6$ EBV DNA copies/μg of DNA. All 6 mice became seriously ill between 5 and 10 weeks after inoculation, with signs of weight loss (figure 1*A*), general inactivity, and piloerection. In contrast, EBV DNA was not detected in the peripheral blood, bone marrow, thymus, spleen, lymph nodes, liver, kidneys, and lungs of 3 control NOG mice that were not transplanted with HSCs but were inoculated with the virus (data not shown). Similarly, no signs of EBV infection were observed in 3 control hNOG mice that were not inoculated with the virus (data not shown). In total, 43 NOG mice that had been humanized with HSCs from 9 different cord blood samples were inoculated with 1×10^3 TD_{50} of EBV, and in 38 of them the results were similar to those observed in the initial 6 mice, with high blood EBV load and severe deterioration in their general condition. Ten of them died and could not be examined further. The remaining 28 mice were killed, and signs of lymphoproliferative disorder were found at autopsy (see the below). These results demonstrate that hNOG mice can be infected with EBV, with a mostly fatal outcome at this virus dose.

EBV-induced lymphoproliferative disorder in hNOG mice. Autopsy of killed mice showed signs of lymphoproliferative disorder typically represented by an overt tumor in the spleen (figure 2*B*). In ~70% (20/28) of the mice autopsied, macroscopical signs of disseminated disease were found in the liver, lymph nodes, or kidneys (figure 2*A* and 2*B*). Seventeen mice were examined pathologically, and 15 of them showed typical histology of diffuse large B cell lymphoma, with remarkable similarity to the human lymphoproliferative disorder in the immunocompromised hosts (figure 2*C*). The tissues contained occasional immunoblasts, Reed-Sternberg–like cells, and Hodgkin-like cells (figure 2*C*). Marked infiltration of large transformed lymphoid cells was also demonstrated in liver, lymph nodes, kidneys, adrenal glands, and lungs (figure 2*C*). Real-time PCR detected high levels ($\sim 1 \times 10^5$ to $\sim 1 \times 10^6$ EBV DNA copies/μg of DNA) of EBV DNA in these organs, and the large transformed lymphoid cells were universally EBV positive by EBER ISH (figure 2*D*). Immunohistochemical analysis showed that the large transformed lymphoid cells were of the activated B cell phenotype, being reactive for CD20 and CD23 and not reactive for CD3 and CD10 (figure 2*D* and data not shown). They were also positive for Mum-1, a late- and postgerminal center cell marker. The EBER-positive cells were CD20-positive B cells (figure 2*D*), and no EBER-positive T cells were identified. Immunostaining revealed that most proliferating cells expressed EBNA2, whereas LMP1 was expressed in only a fraction of them (figure 2*D*). RT-PCR analysis of typical spleen tumors obtained from 3 different mice showed the expression of EBNA1, EBNA2, LMP1, LMP2A, LMP2B; and EBER, consistent with the latency III program of EBV gene expression (figure 2*E*). In addition, transcripts from lytic-cycle EBV genes, including BZLF1 (immediate-early), BMRF1 (early), and BLLF1 (late, encoding gp350/220), were identified (figure 2*F*).

Virus dose–dependent outcome of EBV infection in hNOG mice. To examine the influence of virus dose on the outcome of EBV infection, we inoculated serial dilutions of EBV preparation into 2 lots of hNOG mice, each consisting of 5 mice that had been humanized with the same HSC preparation. Consistent with the results described above, the 4 mice (2 from each lot) that received the higher doses (1×10^3 and 1×10^2 TD_{50}) of the

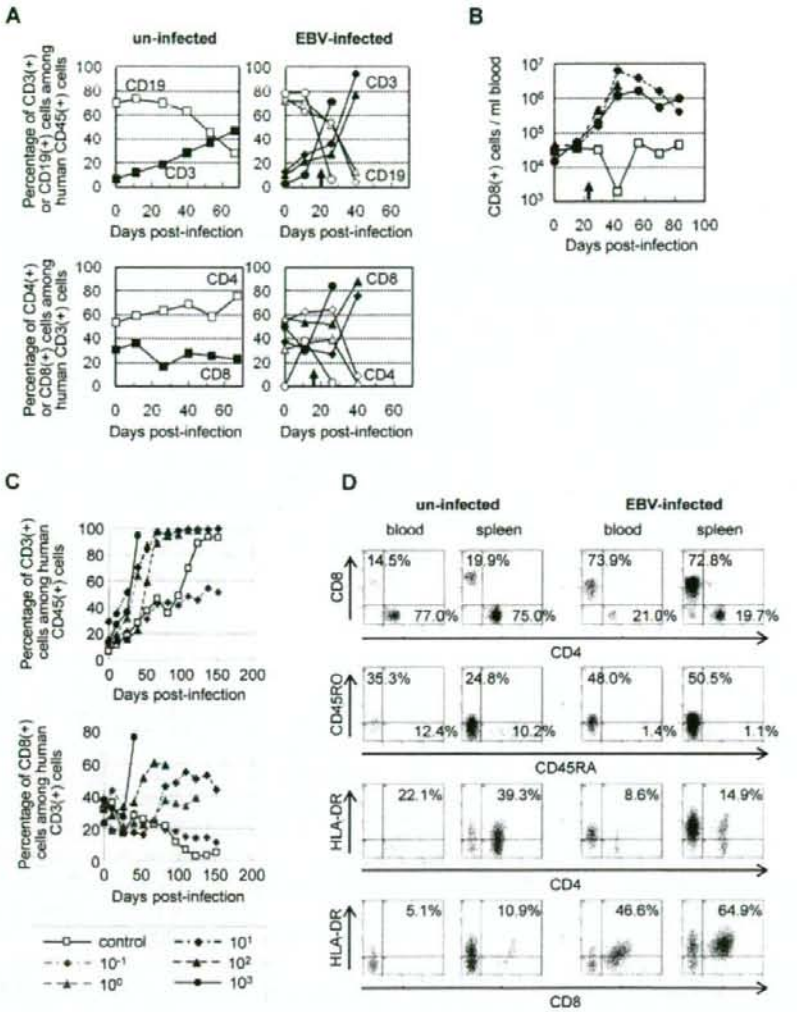

Figure 3. Surface marker expression by peripheral blood T cells in Epstein-Barr virus (EBV)–infected humanized NOG (hNOG) mice. *A*, Changes in the percentages of $CD3^+$ T cells and $CD19^+$ B cells among human $CD45^+$ leukocytes *(upper panels)* and in the percentages of $CD8^+$ cells and $CD4^+$ cells among $CD3^+$ cells *(lower panels)* after infection with EBV. Results obtained from 3 EBV-infected mice and an uninfected mice are shown. White symbols indicate the percentage of $CD19^+$ cells *(upper panels)* or $CD4^+$ cells *(lower panels)*; black symbols indicate the percentage of $CD3^+$ cells *(upper panels)* or $CD8^+$ cells *(lower panels)*. A vertical arrow in the graph area shows the time point at which EBV DNA was first detected in peripheral blood. *B*, Changes in the no. of $CD8^+$ T cells in the peripheral blood of EBV-infected hNOG mice. White symbols indicate uninfected mice, and black symbols indicate infected mice. Note that cell no. is plotted in a logarithmic scale. *C*, Viral dose–dependent T cell responses in hNOG mice inoculated with serially diluted EBV. Ten-fold serial dilutions of an EBV sample starting from 1×10^3 TD_{50} per inoculate were injected intravenously into NOG mice that had undergone transplantation with the same lot of human hematopoietic stem cells (HSCs). Changes in the percentages of $CD3^+$ T cells among human $CD45^+$ leukocytes *(upper panel)* and in the percentages of $CD8^+$ cells among $CD3^+$ cells *(lower panel)* after inoculation with EBV are shown. The viral dose for each mouse is shown in the key. *D*, Comparison of surface marker expression between EBV-infected mice and control mice. Two mice that underwent transplantation with the same lot of human HSCs were either inoculated with EBV or left uninfected; 10 weeks after inoculation, mononuclear cells obtained from peripheral blood or spleen were gated for the expression of human CD3 and then examined for the expression of CD8 and CD4 *(top panels)*, CD45RO and CD45RA *(second from top)*, HLA-DR and CD4 *(second from bottom)*, and HLA-DR and CD8 *(bottom)*.